Application of one-dimensional stagnation solutions to three-dimensional simulation of compact wire array in absence of radiation

Edmund P. Yu, A. L. Velikovich, and Y. Maron

Citation: Physics of Plasmas (1994-present) **21**, 082703 (2014); doi: 10.1063/1.4891844
View online: http://dx.doi.org/10.1063/1.4891844
View Table of Contents: http://scitation.aip.org/content/aip/journal/pop/21/8?ver=pdfcov
Published by the AIP Publishing

PHYSICS OF PLASMAS 21, 082703 (2014)

Application of one-dimensional stagnation solutions to three-dimensional simulation of compact wire array in absence of radiation

Edmund P. Yu,[1,a)] A. L. Velikovich,[2] and Y. Maron[3]
[1]Sandia National Laboratories, Albuquerque, New Mexico 87185, USA
[2]Plasma Physics Division, Naval Research Laboratory, Washington, DC 20375, USA
[3]Weizmann Institute of Science, Rehovot 76100, Israel

(Received 11 June 2014; accepted 18 July 2014; published online 6 August 2014)

We investigate the stagnation phase of a three-dimensional (3D), magnetohydrodynamic simulation of a compact, tungsten wire-array Z pinch, under the simplifying assumption of negligible radiative loss. In particular, we address the ability of one-dimensional (1D) analytic theory to describe the time evolution of spatially averaged plasma properties from 3D simulation. The complex fluid flows exhibited in the stagnated plasma are beyond the scope of 1D theory and result in centrifugal force as well as enhanced thermal transport. Despite these complications, a 1D homogeneous (i.e., shockless) stagnation solution can capture the increase of on-axis density and pressure during the initial formation of stagnated plasma. Later, when the stagnated plasma expands outward into the imploding plasma, a 1D shock solution describes the decrease of on-axis density and pressure, as well as the growth of the shock accretion region. © *2014 AIP Publishing LLC*.
[http://dx.doi.org/10.1063/1.4891844]

I. INTRODUCTION

The wire-array Z pinch is a powerful radiation source that operates on a simple principle: current is driven through a cylindrical annulus of metallic wires in the axial direction (i.e. the z direction), vaporizing the wires while also generating an azimuthal magnetic field B_θ. The resulting radially inward $\mathbf{j} \times \mathbf{B}$ force accelerates the plasma towards axis, where it stagnates, converting its implosion kinetic energy into thermal energy, which is then radiated away (for a visual aid to energy flow in a Z pinch, see the Appendix). Considerable theoretical effort has been put into understanding the stagnation phase, with much of the work devoted to explaining the experimental observation that the radiated energy exceeds the zero-dimensional (0D) estimate of kinetic energy (see Ref. 1 and references therein), possibly through enhanced resistivity,[1,2] ion viscous heating of magnetohydrodynamic (MHD) instabilities,[3] buoyant magnetic bubbles,[4,5] and continued $\mathbf{j} \times \mathbf{B}$ work due to multi-dimensional effects.[6–8]

This work addresses an ostensibly simpler question: How does the implosion kinetic energy convert to thermal energy? Experiments[9,10] suggest that this process is responsible for a significant fraction, if not all, of the "main" radiated power pulse (i.e., the peak of the total and K-shell radiation power, and most of the K-shell radiation yield), at least for wire arrays of sufficiently large diameter.[11] Theoretical models describing this process have existed since the 1950s, and are all either 0D approximating one-dimensional (1D) flow[12–14] or 1D.[15–21]

While such models are excellent for developing physical intuition, the applicability to a wire-array Z pinch is uncertain, owing to its three-dimensional (3D) nature, which is well-documented experimentally.[22–26] At early time, rather than vaporizing into a plasma shell, the wires develop a heterogeneous core-corona structure and undergo a prolonged ablation phase during which cores cook material off their surface, which is then accelerated towards axis by the $\mathbf{j} \times \mathbf{B}$ force. The ablation phase, coupled with an instability on the cores that modulates the ablation rate axially (see Ref. 27, and references therein), results in a 3D imploding and stagnating plasma bearing little resemblance to a cylindrical shell or column. Indeed, recent experimental data[28] suggest significant residual motion in the "stagnated" plasma.

Hence, the relevance of 1D models to 3D wire-array stagnation might seem dubious, due to the complicated flow structures that are only possible in 3D. Nonetheless, scaling laws for the K-shell yields developed using 1D radiation-magnetohydrodynamic (RMHD) simulations (see Refs. 29–32, and references therein) have been consistently successful in predicting the radiative yields and guiding the load design.[33] The same can be said about predicting K-shell yields from, and guiding the design of, Ne and Ar gas-puff Z pinches,[34–36] as well as prediction of thermal neutron yields from deuterium gas-puff Z-pinch loads.[37–39] Very recently, Maron *et al.*[40] found good agreement between a 1D analytical shock model and experimental data obtained both in $\sim$0.5 MA gas-puff implosions observed at the Weizmann Institute of Science and in $\sim$20 MA wire-array implosions at Sandia National Laboratories.

Intuitively, one can expect predictions based on the 1D approach to be applicable to some globally averaged (i.e., averaged over vertical coordinate and azimuthal angle) quantities characterizing the radiative or neutron yield or power only if a large part of the stagnated plasma participates in their generation. This is not always the case—sometimes the relevant radiative output comes from a string of bright spots (which are hot, dense, or both), as, for example, copper K-shell emission in recent wire-array experiments on Z.[41] But

a)Electronic address: epyu@sandia.gov

in many cases, Z-pinch performance is not determined by the small-scale structures, which typically means that a sufficiently large fraction of stagnated mass participates in the relevant emission, as in most of the above-referenced situations to which the 1D-based scalings and models have been successfully applied. Then, the global averaging makes sense. This conclusion refers not only to Z pinches but to a wider class of implosion of interest for inertial confinement fusion and high-energy-density physics. As an example, we quote low-adiabat implosions of cryogenic DT capsules on the Omega laser. Even though these implosions are strongly affected by hydrodynamic instabilities, remarkable shot-to-shot reproducibility of their neutron yields and other observed parameters has been noticed,[42] suggesting some kind of quasi-1D motion.

One should keep in mind, however, that 3D flow is much more complicated than 1D flow, a difference which inevitably affects the globally averaged quantities. For example, local vorticity generated in 3D, which can develop into turbulence, on the average represents an energy sink not present in the 1D description. Shock convergence does not occur along the pinch symmetry axis, as in 1D, but rather in various areas of the stagnated plasma volume, not simultaneously, which means that shock convergence and divergence phases coexist in time, both contributing to the global averaging. All this implies that application of the 1D approximation to the averaged quantities is a non-trivial issue that deserves a special study.

In this work, we consider the applicability of two self-similar, 1D stagnation models to a 3D wire-array simulation. The two models describe a shock and shockless stagnation, respectively, thus covering a broad range of possible scenarios. These models can be helpful in understanding local plasma behavior, but we are more interested in their ability to describe globally averaged plasma properties. In this case, the analytic solutions give us an overarching understanding of the complex fluid motions seen in 3D, and how this kinetic energy converts to internal energy. On a more practical level, the solutions allow us to predict how certain plasma parameters, such as pressure and density, evolve with time. An important related question is if the 1D solutions apply, "How does the 3D fluid motion manifest itself in a 1D description?"

In order to simplify this complicated problem, we focus on a simulation run (essentially) without radiation during the stagnation phase. While this simplification is of course unrealistic, it will enable us to better distinguish between the analytic models, as well as provide a simpler background against which to test our ideas.

Although this work focuses on 3D stagnation of wire arrays, our results may be relevant to gas puffs[43–49] and metallic liners,[50,51] which also develop 3D structures during the implosion phase. Furthermore, recent simulations[52] highlight the important role that 3D hydrodynamics may play during stagnation of inertial confinement fusion capsules.

The paper is structured as follows. In Sec. II, we analyze our 3D simulation results, providing a qualitative description of flows observed in the stagnating plasma and their effect on plasma properties. In Sec. III, we compare the 3D simulation with its 1D "equivalent." In Sec. IV, we briefly review analytical solutions describing shock and shockless stagnation (the details are given in the Supplementary material[53]). In Sec. V and VI, we compare the analytical predictions with the numerical results. In Sec. VII, we make a brief comment on the role of magnetic field at stagnation, followed by a summary in Sec. VIII.

II. 3D SIMULATION OF WIRE ARRAY STAGNATION

A. Simulation description

In this work, we focus on a compact (1 cm radius), 1.15 mg, tungsten wire array on the Z pulsed power generator. We use the 3D MHD code ALEGRA-HEDP,[55] run with thermal and radiative transport (single group implicit Monte Carlo) and allowing for separate ion and electron temperatures. ALEGRA uses high-fidelity equation of state tables and electrical conductivity models,[56] and employs an artificial viscosity to capture shocks (physical ion viscosity is not included). The simulation is run with a Thevenin equivalent circuit representation of Z (see Ref. 23, and references therein), driven with an experimentally determined voltage drive. We only model 7 mm of the full 10 mm axial length of the wire array, for the sake of keeping the number of elements tractable ($\sim 1.7 \times 10^6$). Even so, the simulation is somewhat coarsely resolved, with $dr \sim 20\,\mu$m near axis (graded to 75 μm at r = 2 mm), $dz \sim 60\,\mu$m, and $N_\phi = 120$ cells in the azimuthal direction.

Rather than simulate the discrete wires,[7,8,57] we use a mass inflow boundary condition, motivated and described in Refs. 58 and 59, to model the ablation phase. The idea takes advantage of the fact that the wires play a relatively passive role during the mass ablation phase, acting as stationary mass sources of plasma. In this model, on the cylindrical mass injection surface (located at the wire array's initial radius $R_0 = 1$ cm) each computational cell continuously leaks out mass, which is then rapidly accelerated radially inwards by the $\mathbf{j} \times \mathbf{B}$ force. When an amount of mass equal to the wire array mass has been injected onto the mesh, the mass injection ceases.

We allow axial variation in the mass injection rate, to mimic the aforementioned axial instability on the wires. We also allow blocks of N_c azimuthally adjacent cells to share the same injection rate, to account for the experimental observation that the mass ablation rate may be azimuthally correlated over several wires.[25,60] In this simulation, we assume $N_c = 2$ (i.e., in the notation of Ref. 58, the correlation parameter $C = 1.7\%$), which produced good agreement with experimental backlighting images and radiated power in Ref. 58. Note that in this work, we only consider the limit where there are sufficient wires that the plasma coronas from adjacent wires touch azimuthally, so that there are no azimuthal gaps on the mass injection surface.

Figure 1 presents results of the simulation near the beginning of stagnation, illustrating the precursor mass accumulating on axis, ablated plasma, and the imploding plasma sheath, which sweeps up the ablated plasma. As discussed in Ref. 58, the plasma forms a complicated 3D trailing mass structure behind the imploding bubbles. Unlike a 2D (r,z)

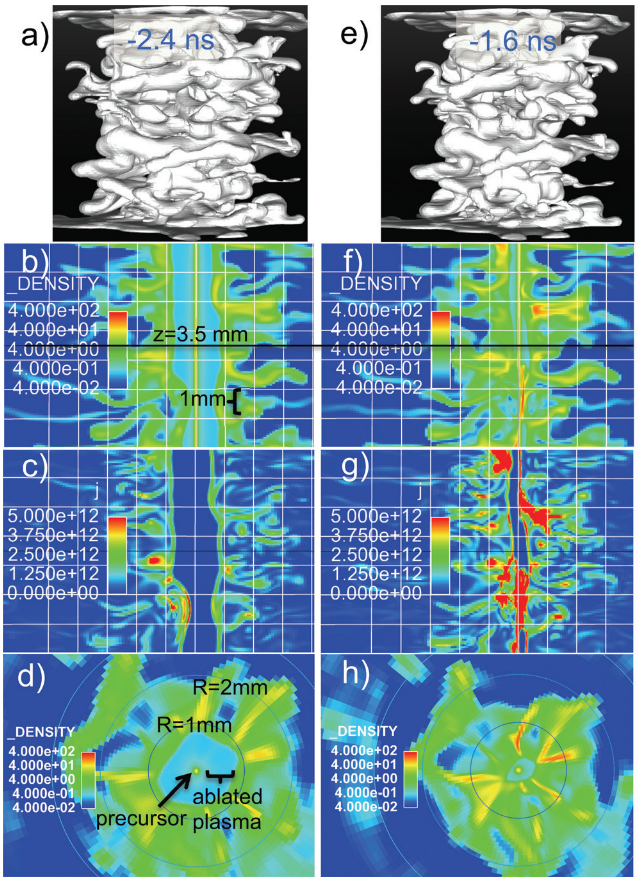

FIG. 1. Example results from the 3D simulation, illustrating density $\rho(\mathrm{kg/m^3})$ and current density $|\mathbf{j}|(\mathrm{A/m^2})$ at two times ($t=0$ corresponds to maximum compression on axis). In (a) and (e), we show a surface of constant density ($1\,\mathrm{kg/m^3}$). The plane shown in (b), (c), (f), and (g) cuts through the center of the simulation domain. The black horizontal line in (b) and (f) is the $z=3.5$ mm midplane, visualized in (d) and (h).

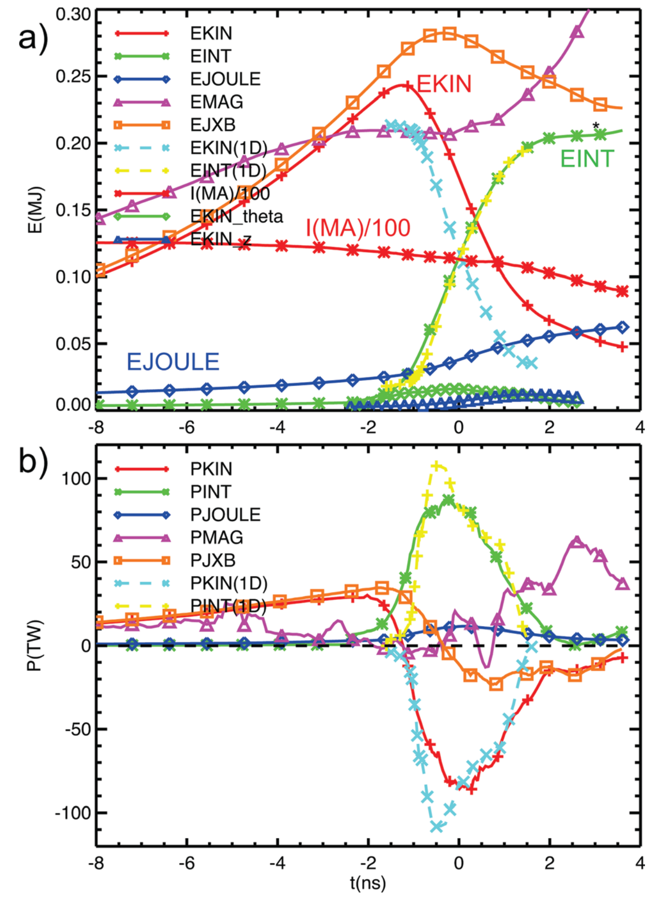

FIG. 2. (a) Kinetic, internal, Joule, and magnetic energy, as well as $\mathbf{J}\times\mathbf{B}$ work and total current I, from the 3D simulation. We also show the azimuthal (EKIN-theta) and axial (EKIN-z) components of kinetic energy. Dashed lines represent kinetic and internal energy from the equivalent 1D simuation, discussed in Sec. III. The initial 1D kinetic energy does not include axial and azimuthal components, and is, therefore, smaller than its 3D counterpart. (b) Corresponding powers.

simulation, in which current flows on the front of the bubbles, in 3D, the trailing mass can support considerable current through azimuthal current paths, as seen in Fig. 1(c), thus leading to reduced growth of magneto Rayleigh-Taylor instabilities (see Ref. 61, and references therein). Hence, while the imploding plasma is highly inhomogeneous, the lack of gross instabilities enhances the chances of 1D theory being able to describe, in an averaged sense, the 3D plasma stagnation. Finally, we introduce a *major* simplification by reducing the plasma opacity by a factor of 10 000 near the start of stagnation (t = −2.4 ns, see Fig. 1). Thus, while the plasma implosion profile is accurately modeled, we effectively turn off radiation losses during the stagnation phase, the global energy balance of which is shown in Fig. 2. Note that all 3D simulation results in the paper refer to the *same* simulation, namely that of a 1.15 mg, 1 cm radius, tungsten wire array.

B. Qualitative description of 3D stagnation

We begin by illustrating the global behavior of the 3D simulation in Figs. 3 and 4, where we plot radial profiles of density $\langle\rho\rangle$, mass-averaged radial velocity $\langle v_r\rangle_\rho$, pressure $\langle p\rangle$, radial ram pressure $\langle p_{ram}\rangle \equiv \langle\rho\rangle\langle v_r\rangle_\rho^2$, magnetic pressure $\langle p_B\rangle \equiv \langle B\rangle^2/2\mu_0$, and mass-averaged ion and electron temperature $\langle T_i\rangle_\rho$ and $\langle T_e\rangle_\rho$. The brackets denote an axial and azimuthal average over a cylindrical surface of constant radius: $\langle\cdots\rangle \equiv \frac{\int \cdots dS}{\int dS}$. Brackets subscripted with ρ denotes a mass-averaged quantity: $\langle\cdots\rangle_\rho \equiv \frac{\int\cdots\rho dS}{\int \rho dS}$. For $t \le 0$ ns, the plasma pressure and density build up on axis as the kinetic energy dissipates. After this time, as seen in Fig. 4, the on-axis pressure and density fall, although the kinetic energy continues to dissipate (see Fig. 2). During this phase of stagnation, the high-pressure plasma core expands outward, colliding into the imploding plasma, as confirmed by the $\langle v_r\rangle_\rho$ profiles.

While the profiles in Figs. 3 and 4 provide a global description of the plasma, to better understand the 3D behavior, we examine plasma flow in a fixed z plane, as shown in Figs. 1(d) and 1(h) and in greater detail in Fig. 5. Although this visualization does not discern axial flows, axial kinetic energy remains a relatively small fraction of the total kinetic

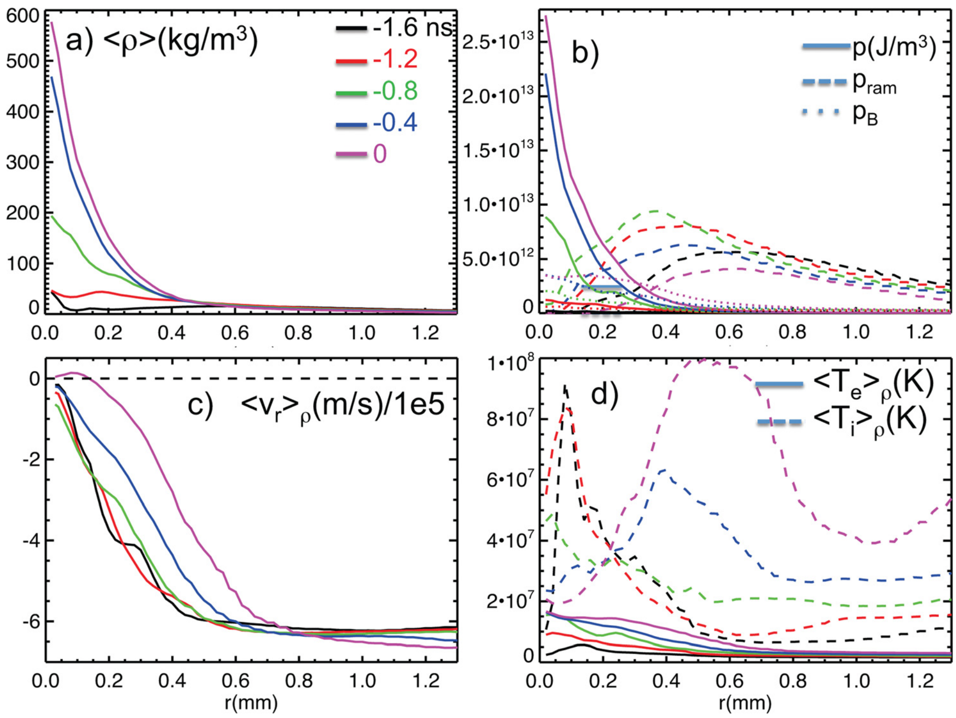

FIG. 3. Axially and azimuthally averaged profiles from 3D simulation during core compression ($t \leq 0$ ns).

energy throughout most of stagnation (see Fig. 2). In Fig. 5, the red-tipped arrows illustrate velocity vectors tangent to the visualization plane, and the purple contour represents $p = 1\text{e}12$ J/m^3, characteristic of "high" pressures achieved in the stagnated plasma.

At $t = -1.2$ ns, the imploding plasma is starting to crush the precursor. Unlike an azimuthally symmetric 1D case, the plasma streams have collided obliquely and off axis (see purple contours), thus partially dissipating kinetic energy while also continuing to implode inward. By $t = -1$ ns, a hot core has assembled on axis. The core will seek to expand outward, due to its high pressure, but it must overcome two effects: the confining magnetic field and the ram pressure $\langle p_{ram} \rangle$ of the imploding plasma, which is the force one would feel, for instance, when standing in front of a firehose. Looking at Fig. 3, the magnetic pressure $\langle p_B \rangle$ is significantly smaller than $\langle p \rangle$ and $\langle p_{ram} \rangle$, so the interplay between the latter two quantities determines core confinement. In Fig. 5, at $t = -1$ the ram pressure is sufficient to confine the core (i.e. it is not re-expanding) over nearly its entirety. However, at the white arrow, the local plasma pressure exceeds the ram pressure, leading to plasma expansion. This "outflow" will

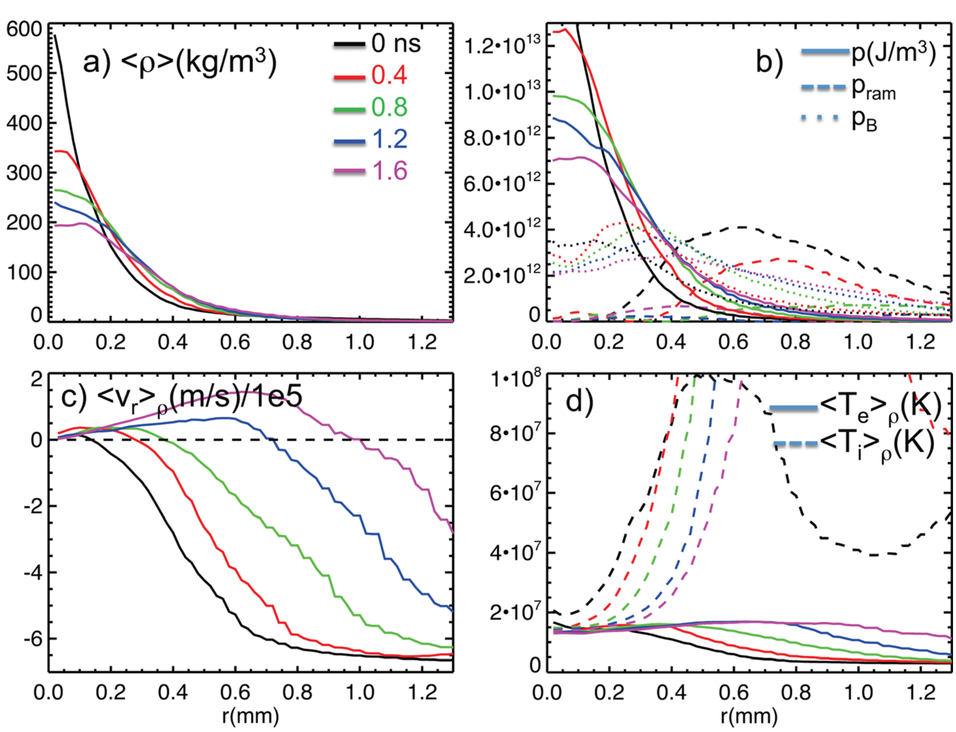

FIG. 4. Axially and azimuthally averaged profiles from 3D simulation during core expansion ($t \geq 0$ ns).

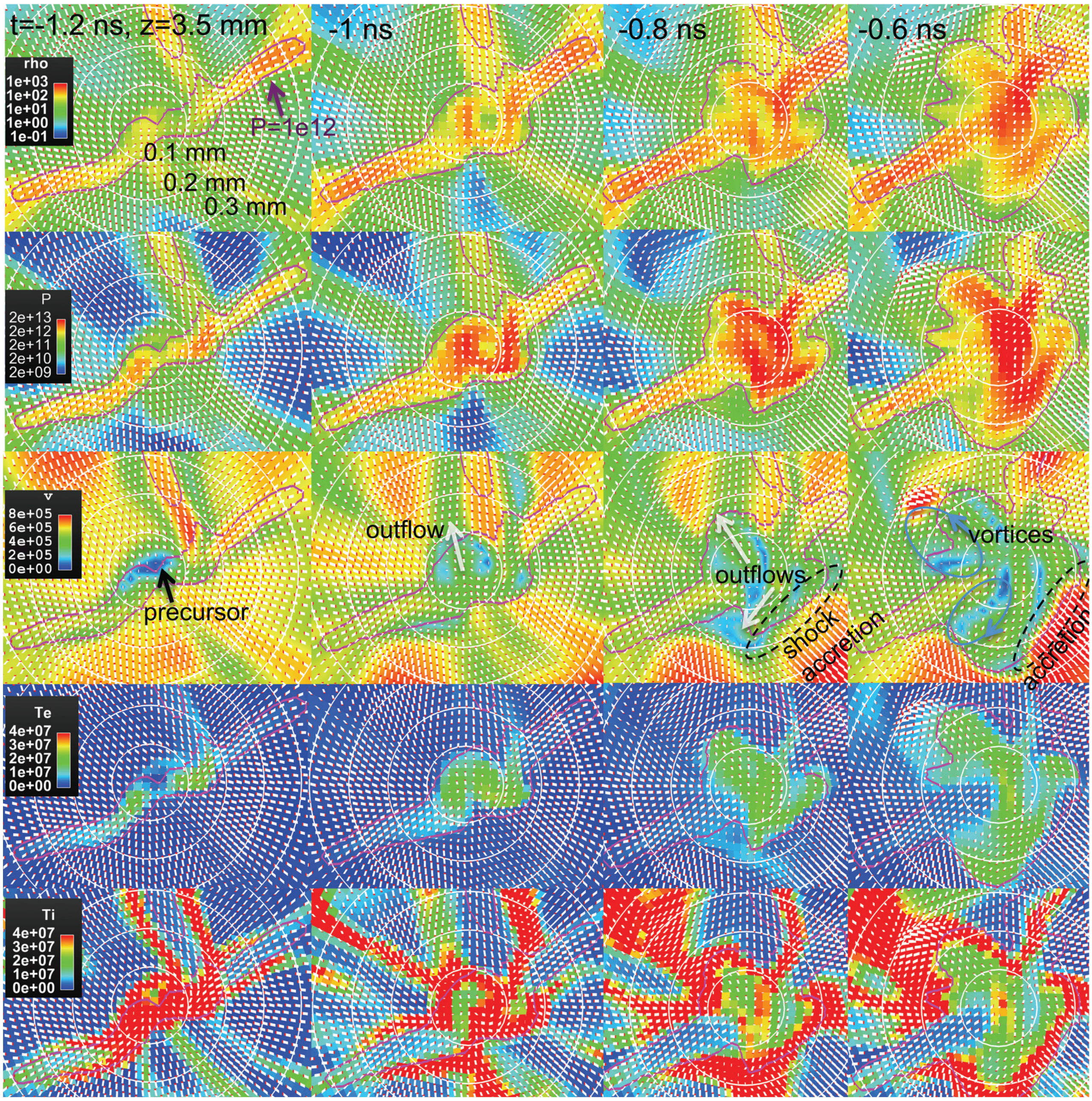

FIG. 5. Plasma flows in the 3D simulation. Plotted are $\rho(\mathrm{kg/m^3}), p(\mathrm{J/m^3}), |\mathbf{v}|(\mathrm{m/s}), T_e(\mathrm{K}), T_i(\mathrm{K})$ in the $z = 3.5$ mm plane, at four different times. Concentric circles represent constant radius contours, spaced 0.1 mm apart. The purple contour represents "stagnated" plasma. Overlaid are velocity vector arrows indicating flow direction by the red tip.

reduce compression in the core, as well as mix the hot, partially stagnated plasma with the cooler, imploding plasma (see Sec. II D).

By $t = -0.8$ ns, outflow has developed on the top and bottom of the core. At this point, the flow in the high-pressure contour resembles two colliding jets, resulting in high-pressure plasma that escapes out the sides.[62] This flow illustrates the inefficiency inherent in stagnation in the absence of perfect symmetry: Even while kinetic energy converts to internal energy, the stagnated plasma simultaneously tries to expand outward against regions of "low" ram pressure, reconverting its internal energy to kinetic energy. However, at $t = -0.6$, we see the outflows redirected inwards via multiple collisions with imploding plasma, thus forming vortices that allow outflow to recompress and restagnate.

In Fig. 5, the purple contour representing the core continuously grows in size, on average. While this growth is partially due to actual plasma expansion (i.e., outflow), primarily, it is due to shock accretion: imploding plasma collides with the core and converts its kinetic energy to thermal energy, thus effectively increasing the mass and size of the core. At $t = -0.8$ ns in Fig. 5, we see evidence of shock accretion in the dashed oval, where high-velocity plasma is brought nearly to a stop upon impact with high-pressure plasma. Consequently, the boundary of the core there grows at $t = -0.6$ ns. We will discuss shock accretion in more detail in Sec. IV A.

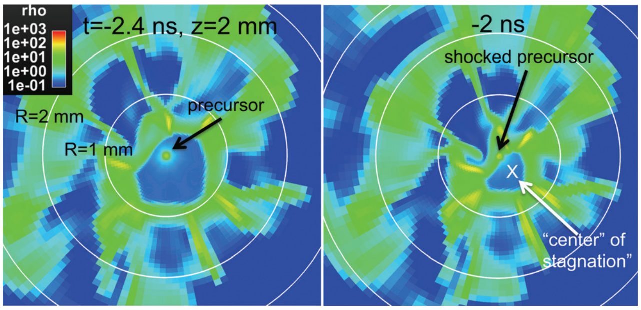

FIG. 6. Off-axis stagnation in the z = 2 mm plane.

In the z = 3.5 mm plane visualized in Fig. 5, the imploding plasma possesses enough symmetry that the core is centered about the axis and precursor plasma. In general, this is *not* the case, as seen in Fig. 6, which shows the start of stagnation in the z = 2 mm plane. At t = −2 ns, we see the imploding plasma sheath will stagnate off axis (roughly at the white 'X'). In this more-common, off-axis stagnation, the ensuing flows are significantly more complicated than those seen in Fig. 5, but exhibit qualitatively similar behavior.

C. γ and γ_{eff}

We have seen that the hot, dense, "stagnated" plasma is not really stagnant at all, consistent with experimental observation.[28] Due to oblique collisions between streams, outflow of high-pressure plasma, and vortex formation, the plasma core retains significant hydrodynamic motion. To better understand the net effect of the flows on energy transport, as well as to connect to the theories in Sec. IV, we discuss the energy equation (cf. Ref. 63)

$$\frac{\rho^{\gamma}}{\gamma-1}\frac{D}{Dt}\left(\frac{p}{\rho^{\gamma}}\right) = -\mathcal{L}, \tag{1}$$

where $D/Dt = \frac{\partial}{\partial t} + \mathbf{v}\cdot\nabla$ is the total derivative and γ is the ratio of specific heats, related to the pressure and specific internal energy e through (cf. Refs. 64 and 65)

$$\gamma = 1 + \frac{p}{\rho e}. \tag{2}$$

Also, $\mathcal{L}$ represents the net effect of all sinks and sources of energy (e.g., thermal conduction, Joule heating, radiation, viscous heating, etc.) In the special case $\mathcal{L} = 0$, we get the usual adiabatic equation

$$\frac{D}{Dt}\frac{p}{\rho^{\gamma}} = 0, \tag{3}$$

which is assumed in the theories in Sec. IV. Because $\mathcal{L} \neq 0$ in general, the range of applicability of the theory is limited. However, in certain cases, even when $\mathcal{L} \neq 0$, the *form* of Eq. (3) is maintained, with a different $\gamma_{eff} \neq \gamma$. In other words, Eq. (1) with $\mathcal{L} \neq 0$ may be equivalent to

$$\frac{D}{Dt}\frac{p}{\rho^{\gamma_{eff}}} = 0, \tag{4}$$

in which case we can still apply the theory, substituting γ_{eff} for γ. Equation (4) implies

$$p(a)/\rho(a)^{\gamma_{eff}} = \mathcal{A}(a), \tag{5}$$

where a denotes a Lagrangian particle and $\mathcal{A}(a)$ is a constant dependent only on a. Using $p = \frac{k_b}{m_i}\rho(T_i + ZT_e)$ in Eq. (5) implies

$$T_i(a) + Z(a)T_e(a) = \frac{m_i}{k_b}\mathcal{A}(a)\rho(a)^{\gamma_{eff}-1}, \tag{6}$$

where m_i is the ion mass and k_b is the Boltzmann constant.

An example of $\gamma_{eff} \neq \gamma$ is provided in Sec. 6.3.7 of Ref. 66, which considers a $\gamma = 5/3$ gas, in the case where $T(a)$ of any given fluid element is maintained constant through external means. Hence, even as the gas expands, dropping its density, $T(a)$ stays fixed. From Eq. (6), we then see that $\gamma_{eff} = 1$ is appropriate.

D. $\gamma_{eff} \sim 1$ and enhanced thermal transport in 3D simulation

In the 3D simulation, $\mathcal{L} \neq 0$, but perhaps, is Eq. (4) applicable? Of particular interest is the axis $r = 0$, where peak density and pressure are attained. If we can describe on-axis plasma with an effective adiabatic exponent γ_{eff}, then Eq. (5) implies $\langle p(r=0)\rangle \propto \langle \rho(r=0)\rangle^{\gamma_{eff}}$. As seen in Fig. 7, from t = −1 to 0 ns, $\langle p(r=0)\rangle$ increases *linearly* with $\langle \rho(r=0)\rangle$, which implies $\gamma_{eff} \sim 1$ is appropriate on axis. Also, from $p = \frac{k_b}{m_i}\rho(T_i + ZT_e)$, we can identify the slope of the line with $\frac{k_b}{m_i}\langle T_i + ZT_e\rangle$ on axis, which is approximately constant during this time interval.

In the absence of energy sources or sinks ($\mathcal{L} = 0$), the temperature in a plasma with $\gamma \sim 1.3$ (appropriate for tungsten in the core) rises as the plasma compresses, following $T \sim \rho^{(\gamma-1)} \sim \rho^{0.3}$. Hence, somehow, the 3D simulation allows temperature on axis to remain fixed rather than rise. One possibility is thermal conduction κ, which diffuses heat from the hot core into the cooler, imploding plasma. In this case, the diffusion of heat outwards is balanced by its convection inwards, as discussed in Ref. 64. The net effect of κ

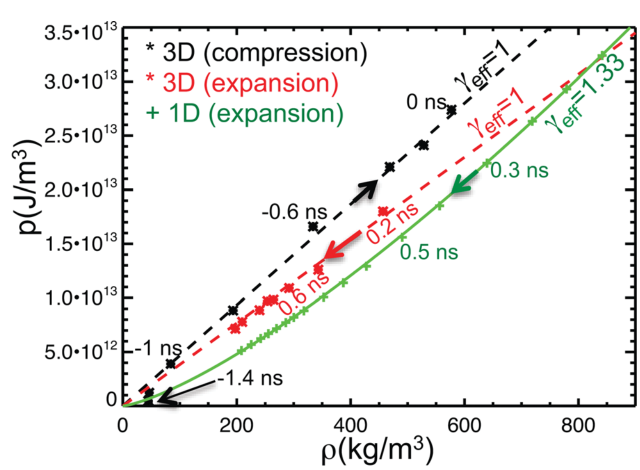

FIG. 7. Axially averaged pressure and density on axis, $\langle p(r=0)\rangle$ and $\langle \rho(r=0)\rangle$, from the 3D simulation, labelled by time. We also show $p(r=0)$, $\rho(r=0)$ from an equivalent 1D simulation, described in Sec. III.

is to allow T_e in the hot core to penetrate into the imploding plasma a distance $l_e \sim \frac{\kappa_e}{\rho c_{V,e}(D+v_i)}$, where κ_e is the electron thermal conductivity; $c_{V,e}$ is the electron specific heat at constant volume; D is the core accretion velocity (see Sec. V B), and v_i is the velocity of imploding plasma. Using "typical" values in the core (i.e., averaged over a r = 100 μm surface), $\langle\rho\rangle \sim 250\,\mathrm{kg/m^3}$, $\langle\kappa_e\rangle \sim$ 3e5W/m $\cdot$ K, $\langle c_{V,e}\rangle \sim$ 9.4e3J/kg $\cdot$ K, $D \sim$ 1.75e5m/s, $v_i \sim$ 8e4m/s, we find $l_e \sim 0.5\mu$m. Since the effective core size $R(t)$ is roughly several hundred μm (see Sec. V B), $l_e \ll R(t)$, and thermal conduction is ineffective at transporting heat away from the core. In this discussion, we have focused on the dominant electron, rather than ion, thermal conduction, which is consistent with unmagnetized ions. Indeed, using $\langle B\rangle \sim 2600\,\mathrm{T}$, $\langle T_e\rangle_\rho \sim 1.4e7\,\mathrm{K}$, $\langle T_i\rangle_\rho \sim 3e7\,\mathrm{K}$, $\langle Z\rangle \sim 60$, $\langle \ln\Lambda\rangle \sim 3.4$, we compute $\Omega_i\tau_{ii} \sim$ 1e–4, $\Omega_e\tau_{ei} \sim 0.7$.

Figure 5 suggests an alternative to κ by which temperature on axis remains constant during core compression. Plasma may transport heat convectively, rather than diffusively, through outflow, which allows hot plasma to expand outward, even though on average the on-axis plasma compresses. The outflow and resulting mixing with cooler, imploding plasma result in an enhanced thermal transport, consistent with the relatively uniform $T_e(r)$ in the core (see Figs. 3 and 4). Note that for a compressing plasma, $\gamma_{eff} \sim 1$ is sometimes used to describe a strongly radiating plasma, which prevents temperature from increasing throughout the plasma. In the 3D case, however, we are claiming $\gamma_{eff} \sim 1$ only near axis. Energy is not lost from the plasma, just transported outwards.

Looking at Fig. 7, from t = 0 to 0.2 ns, ρ and p drop, signifying the beginning of core expansion. During this phase, the ram pressure of imploding plasma is insufficient to confine the core, in an averaged sense. As the core expands, $p(\rho)$ again follows a straight line in Fig. 7, which suggests (i) $\gamma_{eff} \sim 1$ and (ii) $\langle T_i + ZT_e\rangle$ is constant on axis, albeit with a lower value than during core compression. For an adiabatic plasma, $T \sim \rho^{\gamma-1}$, so for $\gamma > 1$, we expect T to fall as ρ decreases. Hence, in order for on-axis temperature to remain constant (i.e. $\gamma_{eff} \sim 1$) during expansion, some heating mechanism must supply energy to plasma on axis. Interestingly, even though a $\gamma_{eff} \sim 1$ plasma prevents the peak temperature from rising during compression, it also maintains temperature on axis during expansion, rather than cooling as in the adiabatic case.

We now consider what mechanism may keep on-axis temperature constant during expansion. In Fig. 4, T_e and T_i are now peaked off axis, so $\kappa\nabla T$ will transport heat towards axis. Another possibility is on-axis Joule heating. However, estimates show both these processes are insufficient to offset pdV cooling during expansion. A likely cause for on-axis heating is once again hydrodynamic motion. Looking at Fig. 8, even though most of the plasma is expanding, we see evidence of "channels" of imploding plasma, which carry hotter plasma from the outer layers directly to the center of the core. These channels supply both internal energy in the form of hot plasma, as well as kinetic energy, which can be dissipated in the core center. The channels are a direct result of the imperfect symmetry.

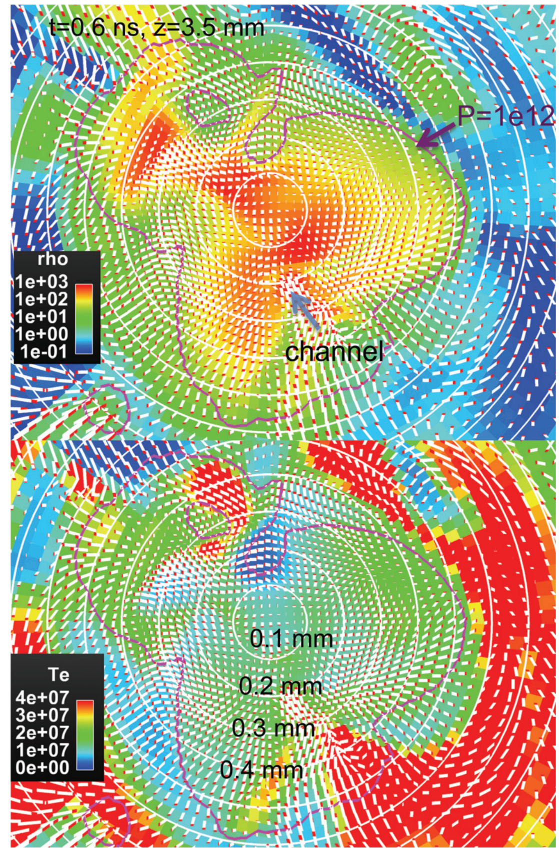

FIG. 8. $\rho(\mathrm{kg/m^3})$ and $T_e(K)$ in the z = 3.5 mm plane, at t = 0.6 ns. The "channel" illustrates a possible heating mechanism even though the core is, on average, expanding.

E. Centrifugal force in 3D simulation

We argued in Sec. II D that complex fluid motion at stagnation allows for enhanced heat transport and thus $\gamma_{eff} \sim 1$, but this is not the only complication introduced by the 3D flows. As seen in Fig. 5, the lack of symmetry during stagnation can result in azimuthal flow, which may affect the overall momentum balance of the stagnated plasma. Taking the radial component of the MHD equation of motion, $\rho\frac{D\mathbf{v}}{Dt} = -\nabla p + \mathbf{J}\times\mathbf{B}$ yields

$$\rho\frac{\partial v_r}{\partial t} = -\frac{\partial p}{\partial r} - \rho\left[v_r\frac{\partial v_r}{\partial r} + \frac{v_\theta}{r}\frac{\partial v_r}{\partial\theta} + v_z\frac{\partial v_r}{\partial z} - \frac{v_\theta^2}{r}\right] + J_\theta B_z - J_z B_\theta.$$

The first two terms on the right-hand side represent forces due to thermal pressure and radial ram pressure, respectively, while the remaining terms in the bracket are due to 3D asymmetry. We will focus on the centrifugal term $\rho v_\theta^2/r$ because of its relative ease of computation; the $\frac{\rho v_\theta}{r}\frac{\partial v_r}{\partial\theta}$ and $\rho v_z\frac{\partial v_r}{\partial z}$ terms involve potentially spiky derivatives, which may require higher resolution simulations to compute accurately.

In Fig. 9, we compare centrifugal force $\langle\rho v_\theta^2/r\rangle$ and radial pressure gradient $-d\langle p\rangle/dr$ at two times. At t = −0.4 ns, which is during the core compression, the two terms are comparable throughout the core, the radial "boundary" of which occurs at the black vertical line (see Sec. V B for how this is defined). Hence, at this time, the radially outward

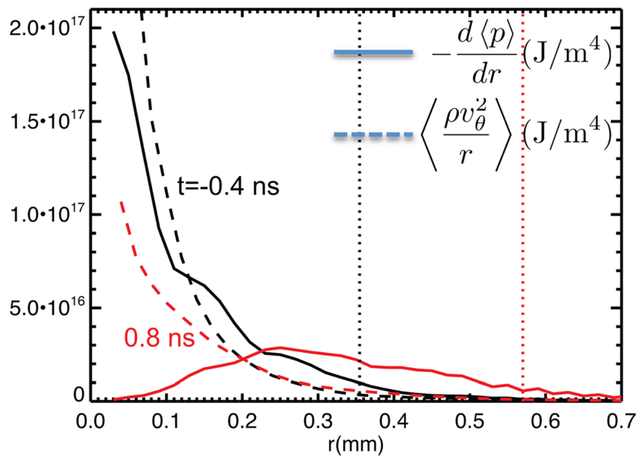

FIG. 9. Axially and azimuthally averaged centrifugal force $\langle \rho v_\theta^2/r\rangle$ (dashed line) and radial pressure gradient $-d\langle p\rangle/dr$ (solid line), at t = −0.4 ns (black) and 0.8 ns (red). The vertical lines represent the boundary of the stagnated plasma, as determined in Sec. V B ($R_{p=1e12}$).

centrifugal force is important in resisting the incoming ram pressure. This observation qualitatively agrees with the experimental analysis of Maron *et al.*,[40] who balanced the ram pressure with both thermal and "hydrodynamic" pressure, associated with residual motion in the shocked plasma.

At later time t = 0.8 ns, which is during core expansion, the pressure gradient exceeds the centrifugal force over much of the core (the boundary of which is denoted by the red vertical line). The diminished role of centrifugal force during core expansion is consistent with the fluid motion in Fig. 8, which does not clearly exhibit the vortices seen earlier. Recall that in Fig. 5, the vortices formed as a result of outflow being redirected inward by ram pressure of incoming flow. However, as seen in Fig. 4(b), the ram pressure profile first rises and then falls with increasing radius. As the ram pressure sampled by the core decreases, it will eventually be insufficient to redirect the outflow back inward, and thus, no vortices form.

III. "EQUIVALENT" 1D SIMULATION

To further assess the impact of 3D effects, we now consider a 1D simulation of a plasma with density, radial velocity, and temperature derived from 3D simulation, just before stagnation (we use the t = −1.6 ns profiles in Fig. 3). How does the resulting stagnation compare to the 3D simulation? These 1D simulations are not entirely equivalent to the 3D case in that we use a finer resolution ($dr \sim 1\,\mu$m as opposed to 20 μm used in 3D) and also set $B = 0$; we will comment on these differences later.

In 3D, the imploding plasma may stagnate off axis, so that precursor plasma does not play a critical role in the stagnation. This is not the case in 1D simulations, where perfect azimuthal symmetry demands that the imploding plasma drive a shock into the precursor plasma, which upon striking axis, reflects outwards before a second shock is driven inwards into the precursor. Eventually, at t ∼ −0.8 ns, the shock reverberation evolves into a single shock traveling through the imploding plasma. In Fig. 10, we compare 1D and 3D simulations at this time. The 1D simulation clearly illustrates shock structure, and results in a denser, smaller, higher pressure core than in 3D. However, the temperatures achieved are more similar, as shown in Fig. 10(d).

Figures 11(a) and 11(b) illustrate the time evolution of 1D density and pressure (measured at the shock front), which peak earlier and higher than ρ and p in 3D (measured on axis). Also, as shown in Fig. 11(d), the 1D shock radius is smaller than its 3D counterpart (see Sec. V B), consistent with off-axis, oblique collisions in 3D resulting in a larger, more diffuse core.

In both 1D and 3D simulations, eventually, the ram pressure of the imploding plasma is insufficient to confine the

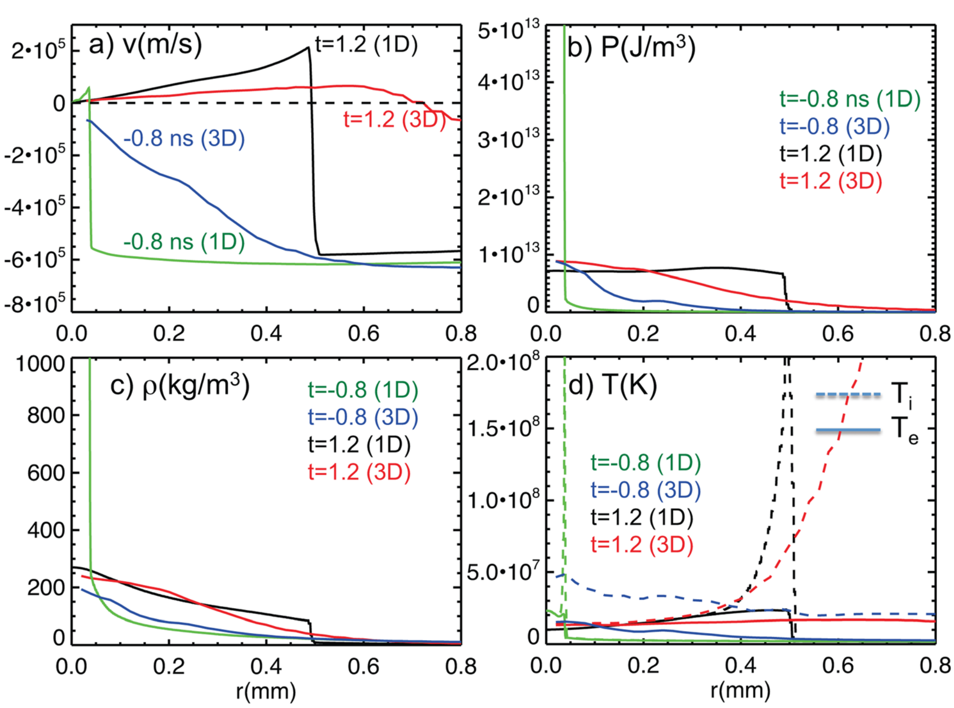

FIG. 10. Comparison between 1D and 3D simulation at t = −0.8 ns and t = 1.2 ns of (a) radial velocity, (b) pressure, (c) density, and (d) electron and ion temperature.

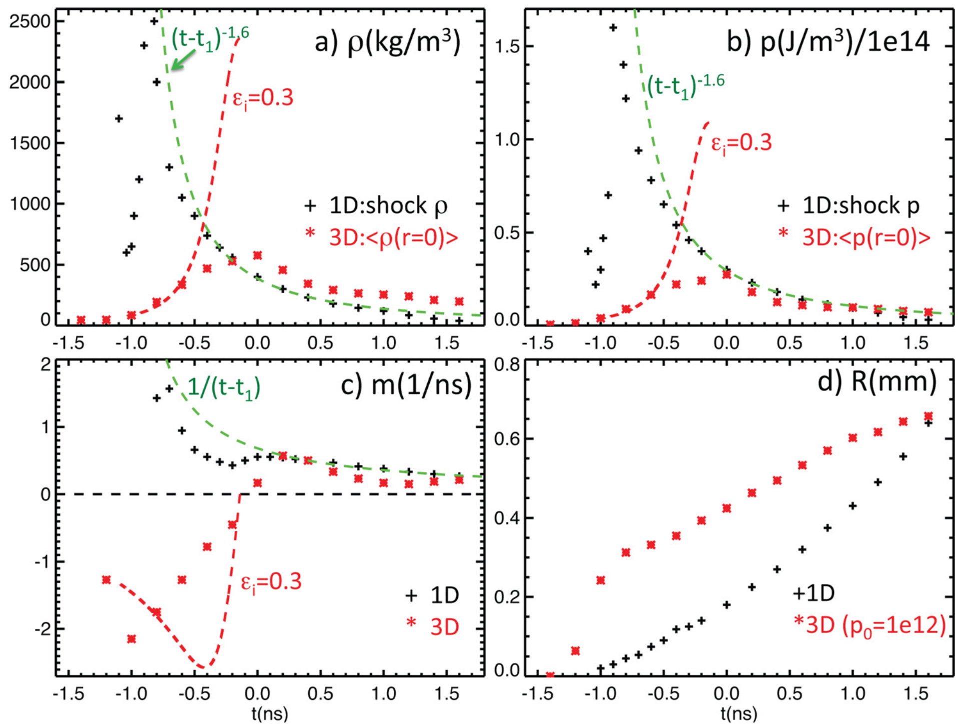

FIG. 11. Comparison between (a) shock density in 1D and on-axis density in 3D, (b) shock pressure in 1D and on-axis pressure in 3D, (c) slope of velocity profile, and (d) shock location in 1D and $R_{p=1e12}$ in 3D. The green dashed line represents predictions from shock theory (Sec. V C), with $t_1 = -1.1$ ns. The red dashed line illustrates predictions from the homogeneous stagnation solution in Sec. VI A.

high-pressure core, which begins to expands outward, colliding into the incoming plasma. During this phase, the decrease in p and ρ in the 1D and 3D simulations follow a similar time dependence. Furthermore, as seen in Fig. 10, at the later time t = 1.2 ns, even the $p(r)$ and $\rho(r)$ from 1D and 3D look more similar, suggesting that effectively the 3D simulation is becoming more 1D-like.

Although the 1D and 3D simulations share similarities during the expansion phase of stagnation, there is also an important difference. Recall from Sec. II C that an adiabatic plasma obeys $p(r=0,t) \propto \rho(r=0,t)^{\gamma}$. In Fig. 7, we plotted $\langle p(r=0,t)\rangle$ vs $\langle \rho(r=0,t)\rangle$ from 3D simulation and found that the adiabatic relation is only satisfied using $\gamma_{eff} = 1 \neq \gamma$; possibly the hydrodynamic flows in 3D result in enhanced thermal transport, thus violating adiabaticity. However, the 1D simulation does not allow 3D flows, so that if thermal conduction is weak, the plasma in the stagnated core is approximately adiabatic during the expansion phase (at earlier time, the core is repeatedly shocked during the shock reverberation, which, of course, is not an adiabatic process). In Fig. 7, we plot $p(r=0,\, t)$ vs $\rho(r=0,\, t)$ from 1D simulation during core expansion. In contrast to 3D, the adiabatic relation $p \sim \rho^{\gamma}$ is indeed satisfied, with $\gamma = 1.33$ rather than $\gamma_{eff} = 1$.

Another difference between 1D and 3D simulations is the efficiency of kinetic energy dissipation. Figure 2 shows that in 1D, 83% of the initial kinetic energy is converted to internal energy during stagnation. Even in 1D, with its perfect azimuthal symmetry, the initial kinetic energy is not completely dissipated, because the core plasma eventually expands into the imploding plasma.

We might expect the kinetic energy dissipation process to be much less efficient in 3D, due to the lack of symmetry in the imploding plasma. Estimating the percentage of kinetic energy converted to internal energy in 3D is complicated by the presence of magnetic field. Not only can B increase the internal energy through Joule heating, it can also add kinetic energy through $\mathbf{J}\times\mathbf{B}$ work (see Fig. 2, $t < -0.4$ ns), as well as *remove* kinetic energy if the plasma does work *on* the magnetic field (see $t > -0.4$ ns). Accounting for these effects, we find that in 3D, from t = −1.4 to 1.6 ns, approximately 66% of the kinetic energy converts to internal energy, which is not drastically lower than in 1D.

We now address the difference in resolution used in 1D and 3D. In 1D, we must resolve the transmitted and reflected shocks driven through the precursor plasma. We found $dr \sim 1\,\mu$m is sufficient, and these simulations appear nearly converged. One might wonder if the 3D simulation also requires such high resolution. However, 3D describes a physically different scenario: in general, the plasma stagnates off-axis, invalidating the picture of shock reverberation through the precursor. Furthermore, the more "messy" stagnation in 3D results in a physically larger core which may not require as high resolution. Indeed, if we increase the resolution from $dr = 20\,\mu$m to $10\,\mu$m, the results are similar, with the peak pressure and density rising by 5% and 8%, respectively, suggesting that $20\,\mu$m resolution is sufficient.

Finally, recall that the 1D simulation discussed here is run with zero current. While we can specify initial (ρ, v_r, T) profiles in ALEGRA, no such option exists for specifying initial current density $j_z(r)$. We can only affect this profile by allowing the magnetic field to diffuse inward for an arbitrary amount of time before the simulation is started. Hence, 1D simulations initialized with non-zero current will possess a different $j_z(r)$ than in 3D, which can result in significant modification to the density and velocity profiles from their 3D counterparts, due to the different $\mathbf{j}\times\mathbf{B}$ forces. Preliminary results indicate even if the initial $j_z(r)$ in 1D is fairly close to that in 3D, the $\mathbf{j} \times \mathbf{B}$ force, which is necessarily radially inward in 1D, is more effective at accelerating material inwards than in 3D, where material in the trailing mass behind the plasma sheath may evolve towards force-free structures,[58] so that $\mathbf{j} \times \mathbf{B}$ is diminished.

IV. SELF-SIMILAR SOLUTIONS FOR COMPRESSION AND EXPANSION OF PLASMAS

Having surveyed the simulations, we now consider a more idealized setting: 1D self-similar solutions. This study will enable us to make quantitative comparison with the qualitative features examined in the Secs II and III. Self-similar solutions often provide a good description of the compression and expansion of shocked fluids. As explained in Ref. 67, this happens because self-similar flow can represent an *intermediate asymptotic* of a more general flow, the stage which is asymptotically approached when, on the one hand, the early-time details of the flow origination are no longer relevant and, on the other hand, the length scales associated with processes that violate self-similarity are still small compared to the global length scale of the flow. There is a wide variety of ideal-gas self-similar shock solutions for planar, cylindrical, and spherical geometries, which include, but are not limited to, the Sedov's blast wave solution and Guderley's collapsing shock solution. These classical solutions are described in detail in monographs.[64,66,68–70] The original Noh's solution in gas dynamics[54] that we are interested in here, as well as its generalizations,[71] belong to the same family, as explained in Ref. 53.

After passage of all shock and expansion waves, a different kind of self-similar flow is asymptotically established. It is characterized by *homogeneous deformation*, which means that the deformation rate tensor $\partial v_i/\partial x_k$ (here the subscripts $i = 1$, 2, 3 correspond to the axes x, y, z) is coordinate-independent, and hence the fluid motion does not generate any shock or sonic perturbations. At this stage, uniform compression and expansion of the fluid are possible. Shockless self-similar solutions of this kind were first studied in gas dynamics by Sedov,[68] and then generalized for MHD in cylindrical geometry in Ref. 15.

Here, we present a brief description of solutions of both kinds, referring the reader to the Supplementary material[53] for details.

A. Noh problem and its self-similar solutions

Consider a cold (i.e. T = 0) plasma of uniform mass density ρ_i and velocity $-v_i$, which is about to stagnate either upon a rigid boundary in planar geometry, as illustrated in Fig. 12(a), or to the axis or center of symmetry in cylindrical and spherical geometry, respectively. The Noh problem, while highly idealized, clearly illustrates the interplay between thermal pressure p of the stagnated plasma and the ram pressure ρv_i^2 of the incident plasma.

Consider the imploding gas as composed of a series of fluid particles, as illustrated in Fig. 12(a). When the first particle strikes the rigid boundary, it comes to a full stop, converting its kinetic energy into thermal energy. Its temperature at stagnation is, therefore,

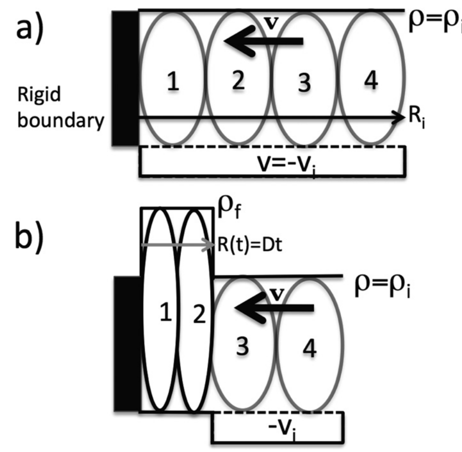

FIG. 12. (a) Initial condition for the Noh problem ($t = 0$). The ovals represent fluid particles constituting the gas, of length R_i. (b) Solution in planar geometry for $t > 0$. Fluid particles 1 and 2 have smashed into the wall, thereby compressing and heating as their kinetic energy converts to internal energy.

$$k_b T_f = \frac{\gamma - 1}{2} m_i v_i^2. \tag{7}$$

The particle stagnates after passing a strong shock wave, in which its density increases to

$$\rho_f = \frac{\gamma + 1}{\gamma - 1} \rho_p, \tag{8}$$

where ρ_p is the pre-shock density, i.e., the imploding plasma density immediately before passing through the shock. From (7) to (8), we find the pressure at stagnation

$$p_f = \frac{\gamma + 1}{2} \rho_p v_i^2. \tag{9}$$

Since v_i equals the mass velocity of the shocked plasma with respect to the cold pre-shock plasma, the speed of the shock wave in the same reference frame equals $v_s = (\gamma + 1)v_i/2$. Relative to the stagnated particle 1 at rest, the outgoing shock front propagates at the velocity

$$D = v_s - v_i = \frac{1}{2}(\gamma - 1)v_i. \tag{10}$$

Particle 2 then crashes into particle 1, which, being at high pressure, brings particle 2 to a stop, so its kinetic energy is also converted into thermal energy. At this point, as illustrated by Fig. 12(b) for planar geometry, we have a hot plasma core (comprised of particles 1 and 2) bounded by imploding plasma (particles 3 and 4).

Despite its high pressure, the core is confined in the sense that velocity is zero there; this confinement is due to the ram pressure $\rho_p v_i^2$ of the imploding plasma. Although the stagnated plasma is not moving, its outer boundary $R(t)$ is nonetheless expanding due to mass accretion at constant velocity $dR/dt = D$, see (10), as the imploding particles immediately adjacent to the core collide into and are stopped by the core. At $t_f = \frac{2}{\gamma+1}\frac{R_i}{v_i}$, the final fluid element (i.e., particle 4 in Fig. 12) has dissipated its kinetic energy, and stagnation is complete. The 1D Noh solution is 100% efficient in converting kinetic energy into internal energy: at $t = t_f$, all the kinetic energy is dissipated. After this time, the hot core will expand outwards through a rarefaction wave, since there is no longer incoming ram pressure to keep it confined.

For planar geometry, the pre-shock density of the cold gas ρ_p is equal to ρ_i, the uniform density of the incident gas at $t = 0$. In cylindrical or spherical geometry, the imploding gas cannot maintain its flat density profile for $t > 0$ due to convergence. One can find the pre-shock density profile from the continuity equation

$$\frac{\partial \rho}{\partial t} + \frac{1}{r^{\nu-1}}\frac{\partial}{\partial r}\left(r^{\nu-1}\rho v\right) = 0, \tag{11}$$

where $\nu = 1$, 2, and 3 for planar, cylindrical, and spherical geometry, respectively. Noting that at zero temperature the density increase due to convergence does not translate into a pressure increase affecting the implosion velocity, we substitute $v = -v_i = \text{constant}$ into (11) and solve the resulting equation with the initial condition $\rho(r, t = 0) = \rho_i$ to obtain

$$\rho(r, t) = \rho_i\left(\frac{v_i t}{r} + 1\right)^{\nu-1}, \tag{12}$$

where $r \geq Dt$. Substituting $r = Dt$ into (12) and using (10), we find the pre-shock density $\rho_p = [(\gamma+1)/(\gamma-1)]^{\nu-1}\rho_i$, and therefore, the stagnated density equals

$$\rho_f = \left(\frac{\gamma+1}{\gamma-1}\right)^{\nu}\rho_i. \tag{13}$$

In the planar case, $\nu = 1$ illustrated in Fig. 12, $\rho_p = \rho_i$, and the total compression described by Noh's solution equals the strong-shock compression (i.e. 4 for $\gamma = 5/3$). For cylindrical and spherical geometry, the total compression equals the strong-shock compression squared and cubed, respectively (i.e., 16 and 64 for $\gamma = 5/3$).

The density, velocity, and pressure profiles characteristic of the Noh's solution are, therefore, self-similar, presented as

$$\frac{\rho(r,t)}{\rho_f} = \begin{cases} 1, & 0 \leq \eta \leq 1 \\ \left(\dfrac{\gamma-1}{\gamma+1}\right)^{\nu}\left[\dfrac{2+(\gamma-1)\eta}{(\gamma-1)\eta}\right]^{\nu-1} & 1 < \eta, \end{cases} \tag{14}$$

$$\frac{p(r,t)}{p_f} = \begin{cases} 1, & 0 \leq \eta \leq 1 \\ 0, & 1 < \eta, \end{cases} \tag{15}$$

$$\frac{v(r,t)}{v_i} = \begin{cases} 0, & 0 \leq \eta \leq 1 \\ -1, & 1 < \eta, \end{cases} \tag{16}$$

where

$$\eta = r/R(t) \tag{17}$$

is the self-similar coordinate.

Basko *et al.*[21] treat a similar problem, including radiation losses. As the losses increase, the shocked plasma cannot maintain the high pressure necessary to withstand the ram pressure of the imploding particles. Hence, the core compresses, thus decreasing the shock accretion velocity D (for strong radiative losses, $D \rightarrow 0$). One of the reasons we turn off radiation in the 3D simulation is to observe nonzero D.

The defining condition of the Noh family of solutions is the requirement that the pre-shock plasma is cold. This constraint cannot be removed without the necessity to analyze the plasma flow at $t < 0$, before stagnation, in which case one has to deal with the Guderley,[64,66,69,70] Rayleigh,[64,66] or some other gasdynamic problem[72] involving a self-similar compression followed by shock reflection. However, one *can* remove the requirements[54] that both the velocity and density profiles at $t = 0$ are flat. Instead, we can assume arbitrary initial power-law profiles[53]

$$\rho(r, t = 0) = \rho_i(r/R_i)^{2\chi}, \tag{18}$$

$$v(r, t = 0) = -v_i(r/R_i)^{-\lambda}, \tag{19}$$

where $\chi > -1$ and $\lambda > -1$ are dimensionless power indices (see Fig. 13(a)). This *generalized Noh* problem, which includes the standard Noh solution as a particular case (i.e. $\chi = \lambda = 0$), is useful for comparison to simulation. For the sake of simplicity, in (18), (19), and all equations that follow, we focus on cylindrical geometry, $\nu = 2$; the planar and spherical case are discussed in Ref. 53.

The shock front initially formed at $r = 0$ propagates outward (see Fig. 13(b)), following a power-law trajectory

$$R(t) = R_i(t/t_m)^{\frac{1}{1+\lambda}}, \tag{20}$$

where t_m is a constant, positive time scale. The shock propagation velocity corresponding to Eq. (20) varies with time

$$D(t) \equiv dR/dt = \frac{R_i}{t_m}\frac{1}{1+\lambda}\left(\frac{t}{t_m}\right)^{-\frac{\lambda}{1+\lambda}}. \tag{21}$$

The self-similar coordinate is still defined by Eq. (17), where $R(t)$ is now given by Eq. (20). We can express the self-similar solution of the generalized Noh problem as

$$v(r, t) = \frac{dR}{dt} \times V(\eta), \tag{22}$$

$$\rho(r, t) = \rho_m(t/t_m)^{\frac{2\chi}{1+\lambda}}G(\eta), \tag{23}$$

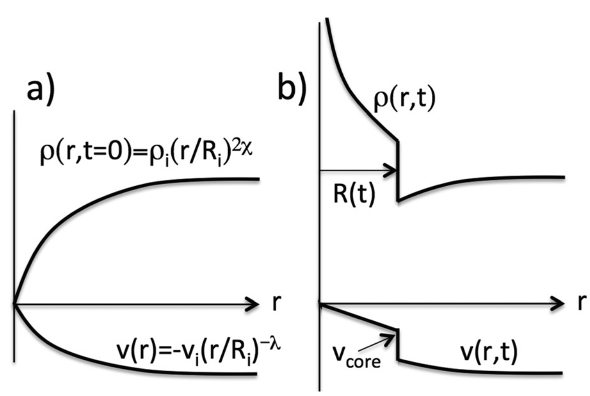

FIG. 13. (a) Initial $\rho(r, t = 0)$ and $v(r, t = 0)$ for the generalized Noh solution. Here $\chi > 0$ and $\lambda < 0$. (b) Shock solution at $t > 0$. Unlike the Noh solution, there is finite velocity inside the shocked plasma (located at $r < R(t)$), with $v(r = R(t)^-) \equiv v_{core}$.

$$p(r,t) = p_m(t/t_m)^{\frac{2(\chi-\lambda)}{1+\lambda}} P(\eta), \tag{24}$$

where ρ_m and p_m are positive, dimensional constants representing density and pressure scales, respectively (in general $\rho_m \neq \rho_i$ in Eq. (18)). The spatial profiles of velocity, density, and pressure are specified by dimensionless functions $V(\eta)$, $G(\eta)$, and $P(\eta)$, respectively.

To develop intuition for how the spatially varying initial profiles alter the standard Noh solution, we consider the initial ram pressure profile

$$p_{ram}(r,t=0) = \rho(r,t=0)v^2(r,t=0) = \rho_i v_i^2 (r/R_i)^{2(\chi-\lambda)}. \tag{25}$$

For $\chi - \lambda > 0$, as is the case illustrated in Fig. 13(a), the initial ram pressure increases with increased radius, and the resulting shock solution is sketched in Fig. 13(b), with nonzero velocity in the core. Recall that in the standard Noh solution,[54] the initial ram pressure profile is flat (i.e. $\chi = \lambda = 0$), and the velocity in the shocked core is zero, cf. Eq. (16), even though its outer boundary is constantly bombarded by the imploding fluid. In the case of $\chi - \lambda \neq 0$, this delicate balance is broken: for increasing ram pressure profile $\chi - \lambda > 0$, as in Fig. 13, the rising p_{ram} felt by the core boundary results in continuous compression of the core, so that $v_{core} \equiv v(r = R(t)^-, t) < 0$. Consequently the plasma pressure in the core continuously rises. Conversely, for $\chi - \lambda < 0$, the initial ram pressure decreases with increasing radius, and $v_{core} > 0$, i.e., now the diminishing ram pressure felt by the core boundary cannot perfectly confine the core plasma, which expands into the imploding plasma.

Hence, even in 1D, it is nontrivial to dissipate all the implosion kinetic energy. While imploding plasma dissipates its kinetic energy as it runs into the shock, simultaneously stagnated core material bounded by the shock front may expand outwards, reconverting its internal energy back into kinetic energy. Global evidence for this behavior was observed in the 3D simulation after t = 0 ns (see Fig. 4).

The compression/expansion of the core when $\chi - \lambda \neq 0$ can have a significant effect on its overall behavior. For instance, the shock velocity D is related to the velocity of imploding plasma entering the shock front, $v(\eta = 1^+)$, by an approximate relation[53]

$$\frac{D}{|v(\eta = 1^+)|} \simeq \frac{\gamma(\gamma-1)}{2\gamma + (\chi-\lambda)(\gamma+1)}, \tag{26}$$

and the total compression of a plasma particle from $t = 0$ till it passes through the strong shock is well approximated by[53]

$$\frac{\rho_s}{\rho_i} \simeq \frac{1}{\gamma(\chi-\lambda+\gamma)} \left[\frac{(\chi+\gamma)(\gamma+1) + (\gamma^2 - 2\gamma - 1)\lambda}{(\gamma-1)(\lambda+1)}\right]^2. \tag{27}$$

For $\chi = \lambda = 0$, Eqs. (26)–(27) are exact and reproduce (10) and (13) (where the post-shock density ρ_s equals the constant density of the core, ρ_f). Otherwise the density peaks at the shock front for $(\gamma-1)\chi + \lambda > 0$ and diverges at the axis for $(\gamma-1)\chi + \lambda < 0$. In the former case Eq. (27) estimates the highest plasma density within the core, and in the latter case, as in Fig. 13(b) – the lowest. Consider, for example, a $\gamma = 5/3$ plasma with initial profiles that correspond to $\chi = 0.25, \lambda = -0.6$, leading to continual core compression. Then Eqs. (26)–(27) yield $D \simeq 0.198|v(\eta = 1^+)|$ and $\rho_f \simeq 122.5\rho_i$. Hence the compression reached by these profiles is larger, and the shock velocity slower, than their flat[54] $\chi = \lambda = 0$ counterpart, for which $D = |v(\eta = 1^+)|/3 = v_i/3$, $\rho_f = 16\rho_i$.

B. Homogeneous stagnation solution

We now consider a shockless stagnation in which plasma compresses uniformly, while converting kinetic energy into internal energy through pdV heating. We discuss the simplest, purely hydrodynamic version of this problem, which may be generalized to include magnetic field,[15–17] radiation,[18] and angular velocity.[73] As above, we focus on cylindrical geometry. The initial condition at $t = -t_i$ is illustrated in Fig. 14(a), in which we have sketched the isothermal solution. As in the shock solution, we consider a row of fluid elements imploding towards axis. However, unlike the shock solution, the elements have finite temperature and pressure, and the velocity profile is linear, which is necessary for shockless compression. In Fig. 14(b), we illustrate the plasma at later time.

Inspecting (19), we note that linear velocity profile would correspond to the value $\lambda = -1$, which is inconsistent with the shock dynamics given by Eqs. (20)–(21). Therefore the solutions reviewed here do not belong to the Noh family

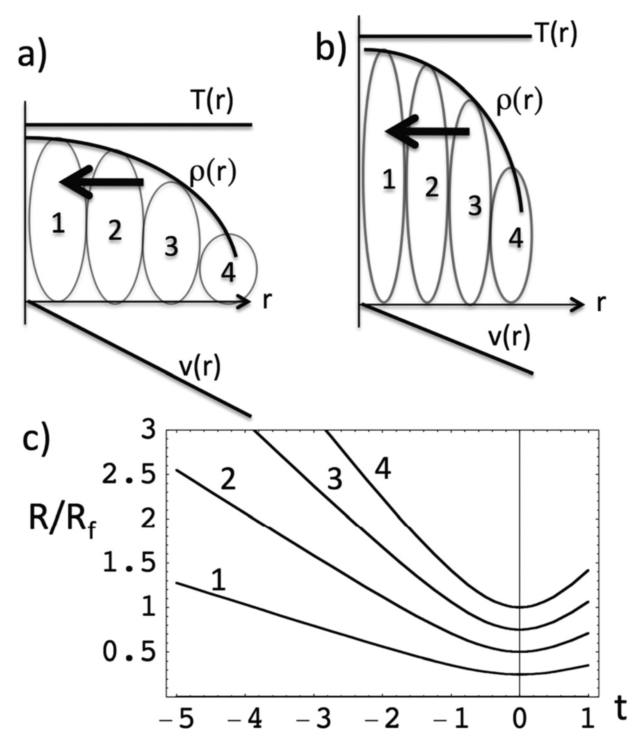

FIG. 14. (a) Initial condition for the isothermal homogeneous stagnation solution ($t = -t_i$). (b) Solution at $t > -t_i$. All fluid elements have compressed and heated as their kinetic energy is converted to internal energy. (c) Sketch of fluid element trajectories. Unlike the Noh solution, here $t = 0$ corresponds to the *end* of stagnation, rather than the beginning.

described in Sec. IV A. Recall that in the shock solution of Sec. IV A, each fluid element travels unimpeded towards axis until it strikes the boundary of the shocked plasma, whereupon its kinetic energy suddenly converts to internal energy. In contrast, in homogeneous stagnation, each fluid element continuously converts its kinetic energy to internal energy, as it does pdV work while compressing the fluid elements in front of it. Hence, as a given fluid element implodes, it gradually slows down (see Fig. 14(c)), and its temperature constantly rises (at least for thermodynamically stable plasma with $\gamma > 1$). At $t = 0$ all fluid particles simultaneously come to rest, signifying the end of stagnation, before expanding at $t > 0$. Like the Noh solution in Sec. IV A, the homogeneous stagnation converts 100% of the initial kinetic energy into internal energy at the end of stagnation.

The definition of the self-similar coordinate (17) does not change, but now the time dependence of the radial length scale $R(t)$ is not a power law, and cannot be prescribed in advance, as in (20), but rather should be determined from the equation of motion. As a consequence of the linear velocity profile, in (22) we have $V(\eta) = \eta$. Hence the self-similar coordinate η has the physical meaning of a Lagrange coordinate of a fluid element, whose radial trajectory can be written as $R(\eta, t) = R_f \eta h(t)$. Here R_f is a characteristic dimensional length scale, for which the outer radius of the plasma column at maximum compression can be chosen. Each fluid element labelled by its Lagrange coordinate η moves according to the same time law $h(t)$, thus allowing all elements to move in unison, as shown in Fig. 14(c), rather than crashing into each other and forming shocks. As a consquence, unlike in the Noh model described in Sec. IV A, there is no shock accretion, and during the stagnation stage the time-dependent length scale of the problem

$$R(t) = R_f h(t) \tag{28}$$

shrinks rather than grows with increasing time.

The governing equations here are the same as in Sec. IV A, ideal-gas equations of continuity, adiabaticity, and motion. But now we seek the self-similar solution in a different form. While Eq. (22) stays the same, with self-similar velocity profile given by

$$v(r, t) = R_f \frac{dh}{dt} \eta = \frac{dh}{dt} \frac{r}{h(t)}, \tag{29}$$

the density and pressure are sought in the form

$$\rho(r, t) = \frac{\rho_f}{h(t)^2} G(\eta), \tag{30}$$

$$p(r, t) = \frac{p_f}{h(t)^{2\gamma}} P(\eta). \tag{31}$$

Here ρ_f and p_f are on-axis density and pressure at the moment of peak compression $t = 0$. The functions $G(\eta)$ and $P(\eta)$, as in Sec. IV A, represent density and pressure profiles.

Equations of continuity and adiabaticity are automatically satisfied by (29)–(31) with arbitrary functions $G(\eta)$ and $P(\eta)$. Separation of variables in the equation of motion imposes a single relation between these two functions, which for our stagnation problem can be expressed as

$$\frac{dP}{d\eta} = -\eta G. \tag{32}$$

Then the time dependence of the normalized length scale $h(t)$ is found from the equation of motion

$$\frac{d^2 h}{dt^2} - \frac{1}{t_0^2 h^{2\gamma - 1}} = 0, \tag{33}$$

where we have denoted

$$t_0 = \sqrt{\frac{\rho_f}{p_f}} R_f, \tag{34}$$

a dimensional constant that plays the role of an effective confinement time, as we will see shortly. Without loss of generality, we can supplement these equations with the initial and boundary conditions

$$h(t = 0) = G(\eta = 0) = P(\eta = 0) = 1. \tag{35}$$

To find a particular solution we have to specify either one of the functions $G(\eta)$ and $P(\eta)$ or a relation between them, and the value of γ. In this work we focus on the isothermal solution with a flat temperature profile, which implies $G(\eta) = P(\eta)$. Then, from (32) and (35), we obtain

$$G(\eta) = P(\eta) = \mathrm{e}^{-\eta^2/2}. \tag{36}$$

Choosing the value of $\gamma = 1$, which is appropriate for isothermal motion in general and for our 3D simulation in particular, see Sec. II D, we solve (33) to obtain

$$\frac{dh}{dt} = \mp \frac{\sqrt{2 \ln h}}{t_0}, \tag{37}$$

$$\mp \frac{t}{t_0} = -\mathrm{i} \sqrt{\frac{\pi}{2}} \mathrm{erf}\left(\mathrm{i}\sqrt{\ln h}\right) = \sqrt{\frac{\pi}{2}} \mathrm{erfi}\left(\sqrt{\ln h}\right), \tag{38}$$

where the upper and lower signs correspond to implosion ($t < 0$) and expansion ($t > 0$) stages, respectively. In (38), $\mathrm{erf}(z)$ is the error function, and $\mathrm{erfi}(z) \equiv \mathrm{erf}(\mathrm{i}z)/\mathrm{i}$ is real and positive if its argument z is. From Eqs. (29) and (37) we determine the time-dependent slope of the velocity profile:

$$m = \partial v / \partial r = v/r = \mp \sqrt{2 \ln h} / (h t_0). \tag{39}$$

In Fig. 15, we plot the normalized trajectory $h(t) = R(\eta = 1, t)/R_f$. The $\eta = 1$ fluid element implodes towards the axis at $t < 0$, gradually slowing down, until at $t = 0$ it comes to a stop at minimum radius R_f. Note that at $t = -t_0$, this fluid particle has reached $r = 1.468 R_f$, i.e., it will not compress much further. Hence, as in Ref. 66, we can roughly identify t_0 as a *confinement time*, during which the fluid is effectively at rest.

To apply the solution for comparison with our simulation, starting from some initial time $-t_i < 0$ we specify the initial density on axis ρ_i, initial pressure on axis p_i, initial radius R_i of the $\eta = 1$ fluid element:

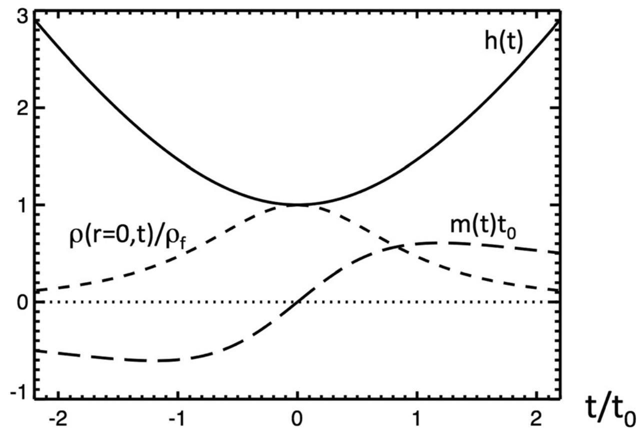

FIG. 15. Normalized trajectory $h(t) = R(t)/R_f$, density on axis, and slope of velocity as functions of time, for $\gamma = 1$, isothermal homogeneous stagnation.

$$R_i = R_f h(-t_i) \equiv R_f h_i, \tag{40}$$

the initial velocity of this element:

$$U_i = R_f \left(\frac{dh}{dt}\right)_{t=-t_i} = -\frac{R_f}{t_0}\sqrt{2\ln h_i} \tag{41}$$

and the initial ratio of thermal energy to kinetic energy of the plasma:

$$\epsilon_i = \frac{\int p dV}{\int \frac{1}{2}\rho v^2 dV} = \frac{2\pi R_f^2 p_f}{2\pi R_f^2 \rho_f \left(\frac{R_f}{t_0}\right)^2 2\ln h_i} = \frac{1}{2\ln h_i} = \frac{p_f}{\rho_f U_i^2}. \tag{42}$$

Here we have used (29)–(31), (36), and (37) to perform the integration.

During stagnation (i.e. $-t_i < t < 0$), the kinetic energy decreases in time as $\ln h(t)$, but the thermal energy remains constant, equal to $p_f R_f^2$. This peculiarity is unique to the $\gamma = 1$ case; for $\gamma > 1$ the internal energy rises while the kinetic energy falls, so as to maintain conservation of energy. Hence $\gamma = 1$ corresponds to a case in which the internal energy gained as a result of converted kinetic energy is immediately lost from the plasma, for instance through radiation. As seen in Sec. II D, the $\gamma = 1$ solution is also relevant to on-axis plasma in the 3D simulation, where rapid thermal transport prevents any increase in the on-axis temperature.

We can now invert Eqs. (40)–(42) to solve for the unknowns: R_f (minimum radius achieved by the $\eta = 1$ fluid element), t_0 (effective confinement time), and h_i (from which we can determine the initial time $-t_i$, via Eq. (38)). Note that the initial time $-t_i$ is not arbitrary, because in this solution we are assuming the stagnation is complete by $t = 0$. Hence, the time interval t_i is the *stagnation time*, i.e., the time it takes for an imploding plasma parameterized by R_i, U_i, ϵ_i to come to a full stop. From Eq. (42) we find

$$h_i = e^{\frac{1}{2\epsilon_i}}, \tag{43}$$

which from (30), (36) determines the peak on-axis density

$$\rho_f = \rho_i h_i^2 = \rho_i e^{\frac{1}{\epsilon_i}}. \tag{44}$$

From Eqs. (40) and (43), we determine the final radius

$$R_f = R_i/h_i = R_i e^{-\frac{1}{2\epsilon_i}}, \tag{45}$$

and from Eqs. (41), (43), and (45) we obtain

$$t_0 = \frac{R_f}{|U_i|}\sqrt{2\ln h_i} = \frac{R_i}{|U_i|}\frac{e^{-\frac{1}{2\epsilon_i}}}{\sqrt{\epsilon_i}}. \tag{46}$$

Finally, Eqs. (38) and (43) determine the stagnation time

$$t_i = t_0\sqrt{\frac{\pi}{2}}\mathrm{erfi}\left(\frac{1}{\sqrt{2\epsilon_i}}\right) = \frac{R_i}{|U_i|}\frac{e^{-\frac{1}{2\epsilon_i}}}{\sqrt{\epsilon_i}}\sqrt{\frac{\pi}{2}}\mathrm{erfi}\left(\frac{1}{\sqrt{2\epsilon_i}}\right). \tag{47}$$

Note the important role played by ϵ_i: smaller ϵ_i (i.e. lower initial pressure) results in deeper compression (Eq. (45)) and higher final density (Eq. (44)), as is reasonable.

V. COMPARISON OF 1D GENERALIZED NOH TO SIMULATION

A. Pre-stagnation profile and caveats

We now investigate if the 1D generalized Noh solution of Sec. IV A can describe aspects of 3D simulation. Recall that this theory requires the density and velocity profiles just before the start of stagnation. In Fig. 3(b), we see that after $t = -1.6$ ns, p starts to rapidly increase on axis, signifying the start of stagnation. Hence we take the profiles at $t = -1.6$, shown in Fig. 16, as appropriate for input into the theory.

Roughly speaking, the profiles can be divided into two phases. In "phase 1," corresponding to $r \le 0.5$ mm, we can fit $\chi \sim 0.25, \lambda \sim -0.6$ (see Eqs. (18) and (19)), so that $\chi - \lambda > 0$. As discussed in Sec. IV A, in this case the increasing ram pressure felt by the core results in continuous compression. In "phase 2," corresponding roughly to $r > 0.8$ mm, $\chi \sim -0.8, \lambda \sim 0$. Now, due to the decreasing ram pressure, shocked plasma expands into the imploding plasma.

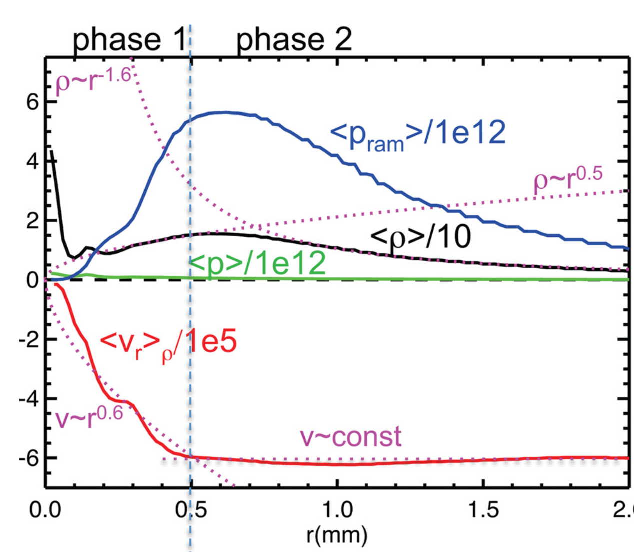

FIG. 16. Axially and azimuthally averaged density $\langle\rho\rangle$ (kg/m^3), pressure $\langle p\rangle$ (J/m^3), radial velocity $\langle v_r\rangle_\rho$ (m/s), and ram pressure $\langle\rho\rangle\langle v_r\rangle_\rho^2$ (J/m^3) at $t = -1.6$ ns. Dashed purple curves are power-law fits to density and velocity.

Before comparing theory with simulation, we must point out some complications. First, the shock theory described in Sec. IV A assumes a cold (i.e. $T_i = T_e = 0$) imploding plasma, whereas here the imploding plasma possesses a finite temperature and pressure, which will reduce shock compression. However, because the Mach number of the imploding plasma is fairly high (≥ 5), we are close to the strong shock limit assumed in the theory.

Second, the shock theory doesn't account for a precursor plasma on axis, which is clearly seen in Fig. 16. However, as seen in Fig. 6, in 3D simulation the stagnation usually occurs off axis, so that in the case of a small precursor (as is the case here), the precursor may not play an essential role in determining the stagnation conditions. Hence we will attempt to apply the generalized Noh solution to the 3D simulation, ignoring the precursor on axis.

Third, theory assumes the adiabatic energy equation (3) holds throughout the shocked plasma, with γ defined by Eq. (2). However, we have seen in Sec. II D that on axis, in 3D simulation it is more appropriate to use $\gamma_{eff} \sim 1 \neq \gamma \sim 1.3$. Therefore, whereas theory requires only a single value of γ, in 3D simulation we must consider 2 values: γ_{eff} (which determines $p/\rho^{\gamma_{eff}} = \text{const}$ on axis) and γ (which determines the shock jump $\rho_2/\rho_1 = (\gamma+1)/(\gamma-1)$ at the core boundary). This complication will alter those expressions which depend on γ, such as Eqs. (26) and (27). However, those predictions which are independent of γ remain valid.

B. Shock boundary R(t) in 3D

A signature of the shock solution is the continuous growth of the shock boundary $R(t)$. However, we cannot discern a well-defined shock boundary in the averaged profiles in Figs. 3 and 4. Although we have seen shock accretion-like behavior in Fig. 5, because the shocks occur at different locations at a given time, the averaged profiles vary gradually.

Recall the intuitive picture behind the generalized Noh problem: plasma stagnates on axis, forming a core of sufficient pressure that it can resist the incoming ram pressure, thus allowing the core to grow through accretion. Although we cannot discern a shock discontinuity in Fig. 17(a), we notice that the $\langle p(r)\rangle$ profile grows in the sense that the radial location of the intersection of $\langle p(r)\rangle$ with a fixed value p_0, which we denote by $R_p(t)$, increases with time (i.e., R_p satisfies $\langle p(R_p)\rangle = p_0$). In Fig. 17(a), we show the location of $R_p(t)$ for $p_0 = 1e12\,\mathrm{J/m^3}$, which is on order the incoming ram pressure (see Fig. 16). In the absence of a discernable shock, we use $R_p(t)$ as a measure of the shock boundary.

In Fig. 17(b), we plot $R_p(t)$ for several values of p_0. All $R_p(t)$ show qualitatively the same behavior, rising rapidly before reaching a stage of linear growth. At late enough time, we see $R_p(t)$ saturate. To understand this, recall R_p grows through shock accretion: imploding plasma impacts upon the plasma core, converting to stagnated plasma with pressure $p_s \geq p_0$. However, during phase 2, the ram pressure of imploding plasma is decreasing, and since the stagnated plasma pressure p_s is on order p_{ram} (see for instance Eq. (9)), eventually, $p_s < p_0$. At this point, R_p can no longer grow: the

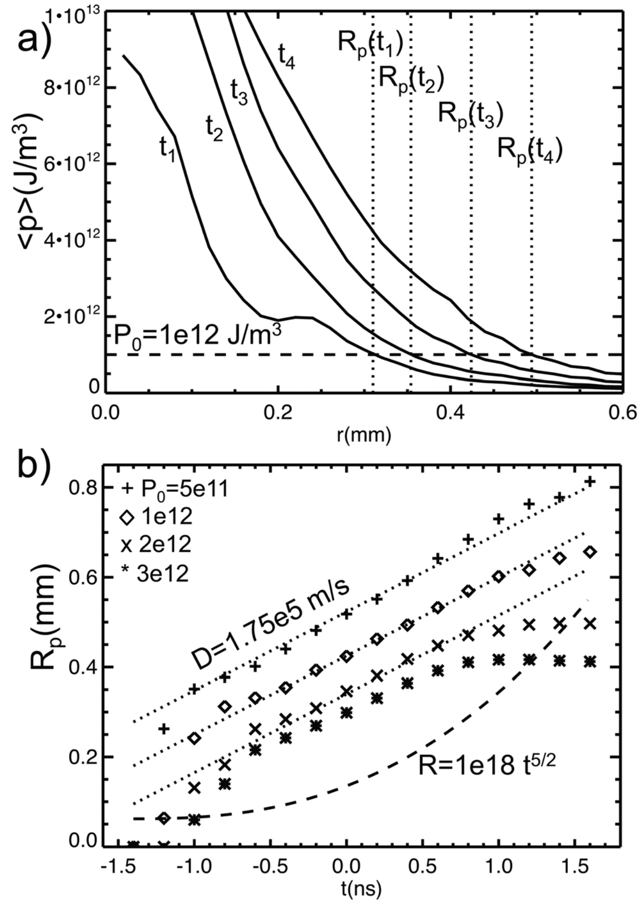

FIG. 17. (a) Axially and azimuthally averaged pressure $\langle p\rangle$ at times $t_1 = -0.8\,\mathrm{ns}$, $t_2 = -0.4$, $t_3 = 0$, $t_4 = 0.4$. The intersection of $\langle p(r)\rangle$ with p_0 defines $R_p(t)$. b) $R_p(t)$ for various values of p_0. Dotted lines show $dR_p/dt = D = 1.75e5\,\mathrm{m/s}$.

accreting plasma does not have sufficient pressure to be detected by $R_{p=p_0}$.

The generalized Noh solution predicts $R(t) \propto t^{\frac{1}{1+\lambda}}$ (see Eq. (20)), which in phase 1 ($\lambda = -0.6$) implies $R(t) \propto t^{5/2}$. More specifically, the theory yields $R(t) = 1e18 t^{5/2}$ (where R and t are measured in meters and seconds, respectively), shown in Fig. 17(b). The growth shown in 3D simulation is much faster, and the time dependence is qualitatively different from $t^{5/2}$. Hence, the shock solution does not provide an adequate description of the phase 1 $R(t)$. This is reasonable: during phase 1, in 1D cylindrical geometry a very compact, high density core is formed. In 3D, the lack of symmetry results in a much larger, lower density core, with effectively larger $R(t)$. This is due not only to plasma striking off axis but also plasma expanding through outflows.

At $t = -0.8\,\mathrm{ns}$, peak p_{ram} is reached in 3D, and the subsequent decrease in p_{ram} signifies the start of phase 2 ($\lambda = 0$). For this phase, we expect linear growth in $R(t)$, although we also expect a transition period during which the solution switches from phase 1 to phase 2. Indeed, by $t \sim -0.6\,\mathrm{ns}$, R_p shows linear growth. The shock velocity $D = dR_p/dt$ varies slightly depending on the value of p_0 used to define $R_p(t)$, but $D = 1.75e5$ m/s provides a reasonable overall fit. To compare this value to the shock theory, we assume that the plasma is described by a single value of $\gamma = 1.32$. Plugging

$\chi = -0.8, \lambda = 0, \gamma = 1.32, v(\eta = 1^+) = 6e5\,\mathrm{m/s}$ into Eq. (26) yields $D = 3.2e5$ m/s, considerably faster than the observed value, which is reasonable. As mentioned earlier, theoretical results that depend on γ are not accurate, because theory assumes that the plasma can be defined by a single γ. However, as seen in Sec. II D, this is not the case, and the lower effective value of on-axis γ will result in a lower D.

C. On-axis $\rho(t)$, $p(t)$, and $m(t)$ in 3D

As mentioned in Sec. V A, the presence of γ and γ_{eff} precludes the use of theoretical predictions that depend on γ. Nonetheless, from Eqs. (20), (23), and (24), the shock theory allows us to predict how $\rho(t)$ and $p(t)$ evolve at a fixed value of $\eta = r/R(t)$. For instance, at the shock front $R(t)$, $\eta = 1$ so that $\rho(R(t)) = \rho_m h(t)^{2\chi} G(\eta = 1) \propto t^{\frac{2\chi}{1+\lambda}}$ and $p(R(t)) \propto t^{\frac{2(\chi-\lambda)}{1+\lambda}}$. Since these results are independent of γ, we expect they remain valid even in the 3D simulation.

Unfortunately, as mentioned earlier, the 3D-averaged profiles in Figs. 3 and 4 do not exhibit a well-defined shock, preventing us from following $\rho(t)$, $p(t)$ there. Nonetheless, we can clearly define $\rho(t)$, $p(t)$ at $r = 0$, corresponding to $\eta = 0$. In the approximate analytic solution to the generalized Noh problem, $P(\eta) \approx$ constant for $\eta < 1$, so that $p(r,t)$ is spatially flat in the shocked plasma. In this case, Eq. (24) predicts that at $r = 0$ (or any $r < R(t)$), $p(r = 0, t) \propto t^{\frac{2(\chi-\lambda)}{1+\lambda}}$.

In the same analytic approximation, the density profile $G(\eta) \propto \eta^{\frac{2[(\gamma-1)\chi+\lambda]}{(\chi-\lambda+\gamma)}}$, so except for the special case, $(\gamma-1)\chi + \lambda = 0$, $G(\eta = 0)$ is either zero or infinite. In the case where $G(\eta = 0) \to \infty$, in 1D simulations, the density on axis increases faster than the predicted $t^{\frac{2\chi}{1+\lambda}}$, as it asymptotes towards infinity. Finite thermal conductivity, not accounted for in theory, will tend to smooth out the density profile $G(\eta)$, and recover $\rho(r = 0, t) \propto t^{\frac{2\chi}{1+\lambda}}$.

Finally, in the analytic approximation, $V(\eta) \simeq \eta$ in Eq. (22), so $v(r)$ is linear in the shocked plasma. Hence, another comparison we can make is how the slope of the velocity m evolves in time. From (20)–(22), we find

$$m(t) \propto 1/t. \tag{48}$$

As discussed in Sec. V A, the non-monotonic ram pressure profile suggests stagnation will occur in two phases. During phase 1 ($\chi = 0.25$, $\lambda = -0.6$), the increasing ram pressure results in continuous compression of the stagnated plasma: $p \propto t^{\frac{2(\chi-\lambda)}{1+\lambda}} \sim t^{4.25}$, $\rho \propto t^{\frac{2\chi}{1+\lambda}} \sim t^{1.25}$. In Fig. 18, we compare these predictions to $\langle\rho(r = 0, t)\rangle$, $\langle p(r = 0, t)\rangle$, $m(t)$ from 3D simulation, and find unconvincing agreement. Most likely, the initial formation of the stagnating core in 3D, which involves oblique and off-axis collisions, does not possess enough azimuthal symmetry to be described by a 1D shock.

During phase 2 of stagnation ($\chi = -0.8, \lambda = 0$), shock theory predicts the stagnated plasma expands into the imploding plasma, so that both the pressure and density on axis fall as $t^{-1.6}$. As seen in Fig. 18, these predictions agree much better with the 3D simulation. Unlike phase 1, during phase 2, a fairly "large" (relative to the imploding plasma profile), high pressure core has already formed on axis, allowing the 1D shock theory to be more easily realized.

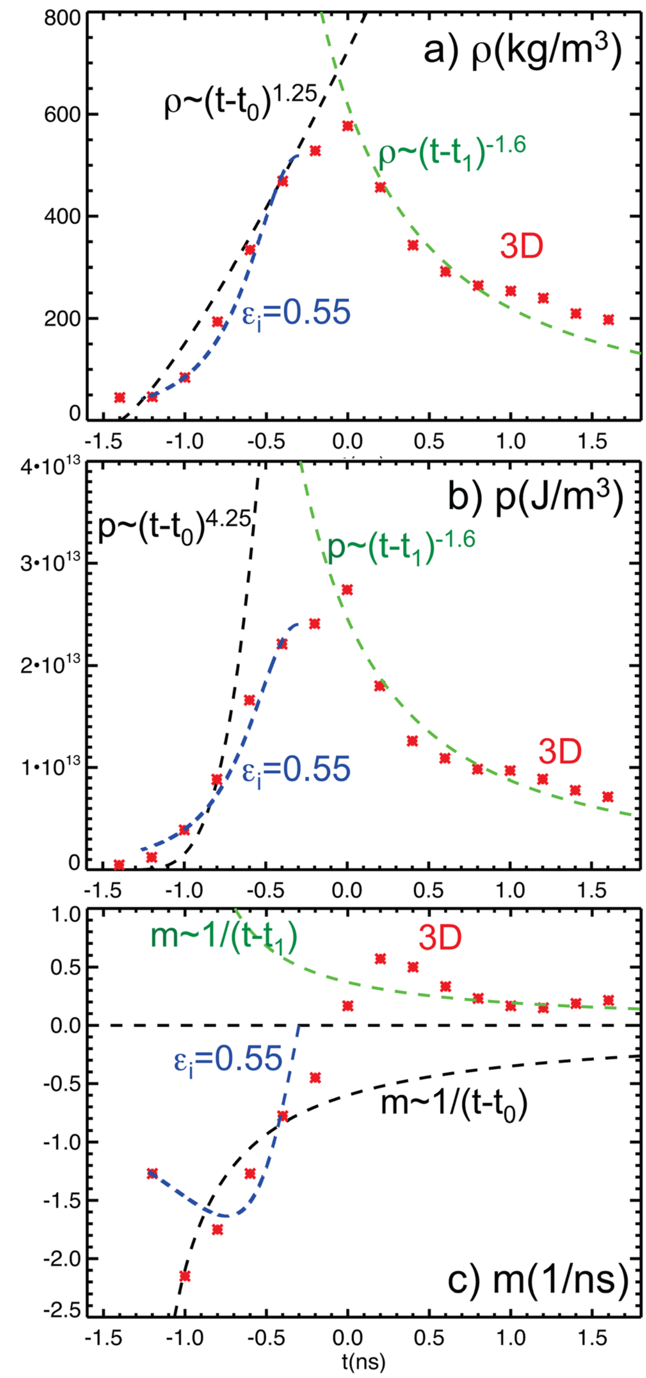

FIG. 18. $\langle\rho(r = 0, t)\rangle$, $\langle p(r = 0, t)\rangle$, and slope of mass-averaged radial velocity from 3D simulation are shown in red. Black and green curves are power-law fits predicted by shock theory, with $t_0 = -1.4$ ns and $t_1 = -1.1$ ns. The blue curve illustrates the homogeneous stagnation solution (see Sec. VI B).

D. Comparison of generalized Noh to 1D simulation

One might expect the generalized Noh solution to be more applicable to the 1D equivalent simulation, which is free from 3D effects. However, as described in Sec. III, the initial stagnation involves a reverberating shock driven through the plasma precursor. This behavior is beyond the scope of the Noh solution, which only treats a single outward-propagating shock.

Eventually, the shock reverberation transitions to a single shock, and we can apply the theory. By this time (t = −0.8 ns), the compression phase has just completed, and the core starts to expand in response to the decreasing ram pressure, in accordance with phase 2 of stagnation. As seen in Figs. 11(a) and 11(b), the shock density and pressure in 1D eventually settle onto the $t^{-1.6}$ solution predicted by the theory. Also, in Fig. 11(c), $m(t)$ obeys the predicted $1/t$ solution (48) after a transition period. These observations suggest that after a compression phase that is not described by the generalized Noh solution, both 1D and 3D simulations transit to an expansion phase of stagnation, which is well-described by the theory.

VI. APPLICATION OF HOMOGENEOUS STAGNATION SOLUTION TO 3D SIMULATION

A. $\gamma_{eff} \sim 1$, isothermal homogeneous stagnation solution

As seen in Sec. V C, the generalized Noh solution does not accurately describe the compression phase of 3D stagnation. This discrepancy is not surprising, since in the shock solution, the fluid striking the stagnated core dissipates nearly all its kinetic energy owing to perfect azimuthal symmetry. In contrast, in 3D, the fluid may collide obliquely and off axis, thus resulting in a high pressure core which retains significant residual motion. Furthermore, as seen in Fig. 3(c), this motion is characterized by a nearly linear $\langle v_r(r)\rangle_\rho$. These properties suggest that the homogeneous stagnation of Sec. IV B may be applicable.

As noted in Ref. 66, the homogeneous stagnation solution comes in many flavors: the solution can describe plasma that is isothermal, isentropic, etc. To understand what type of solution is appropriate for application to 3D simulation, we plot the total temperature profile $\langle T_t\rangle \equiv \langle T_i + ZT_e\rangle$ (computed via $\frac{\langle p\rangle}{\langle \rho\rangle}\frac{m_i}{k_b}$) in Fig. 19. After a rapid rise on axis due to the initial shock interaction, $\langle T_t\rangle$ spreads outward (which we argued in Sec. II D was due to convective outflow and mixing) while its peak value remains relatively constant. Hence, during the compression phase $t \le 0$ ns, the stagnating plasma appears to evolve towards the isothermal solution, with $\langle T_t(r)\rangle = T_0$, a constant in space *and* time, approximately equal to its value on axis $\langle T_t(r=0)\rangle$.

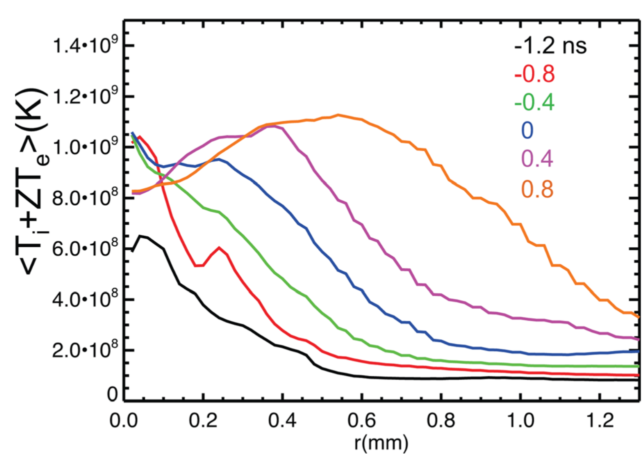

FIG. 19. $\langle T_i + ZT_e\rangle$ from 3D simulation.

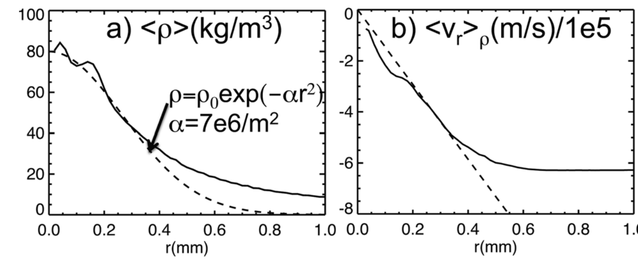

FIG. 20. $\langle \rho\rangle, \langle v_r\rangle_\rho$ from 3D simulation at t = −1 ns (solid) and theoretical profiles from isothermal, homogeneous stagnation solution (dashed).

The time independence of T_0 determines the effective adiabatic index γ_{eff} as discussed in Sec. II C. From Eq. (6), the temperature increases with rising density as $T_t \propto \rho^{\gamma_{eff}-1}$. Because T_0 is relatively constant during the compression phase, $\gamma_{eff} \sim 1$, as argued in Sec. II D. Therefore, we will apply the $\gamma_{eff} \sim 1$, isothermal homogeneous stagnation solution to the 3D simulation.

This solution predicts a Gaussian density profile (36) and linear velocity profile (29). In Fig. 20, we plot $\langle \rho\rangle$ and $\langle v_r\rangle_\rho$ from 3D simulation at t = −1 ns, early in the compression phase of stagnation, along with theoretical fits from the isothermal solution. The agreement is reasonable for $r \le 0.3$ mm. Let us see how the theoretical profiles will stagnate compared to the 3D simulation.

Recall from Sec. IV B that to utilize the stagnation solution, at initial time $-t_i$ we must specify R_i (see Eq. (40)), U_i (41) and ϵ_i (42). We can determine R_i from Eqs. (17), (30), and (36), which predict that at initial time $-t_i$, $\rho(r,-t_i) = \frac{\rho_f}{h(-t_i)^2} e^{-\frac{1}{2}\left(\frac{r}{R_i}\right)^2}$. Figure 20(a) implies $\alpha \equiv 1/(2R_i^2) = 7e6/m^2$, so $R_i = 0.267$ mm and $U_i = v_r(R_i) = -3.9e5$ m/s. To determine ϵ_i we recall from Eq. (42)

$$\epsilon_i = \frac{p_f}{\rho_f U_i^2} = \frac{p_f/h(-t_i)^2}{\left(\rho_f/h(-t_i)^2\right) U_i^2} = \frac{p(r=0,-t_i)}{\rho(r=0,-t_i)U_i^2} \equiv \frac{p_i}{\rho_i U_i^2} \tag{49}$$

where in the second to last equality we have used Eqs. (30) and (31), with $\gamma = 1$, to relate the maximum on-axis pressure p_f and density ρ_f to the initial pressure p_i and density ρ_i. Choosing the initial time $-t_i$ to correspond with −1 ns in the 3D simulation, we obtain from 3D simulation $p_i = 3.9e12\,\mathrm{J/m^3}$ and $\rho_i = 84.2\,\mathrm{kg/m^3}$, so that $\epsilon_i \sim 0.3$.

With the parameters R_i, U_i, ϵ_i, we can determine how the isothermal, $\gamma_{eff} = 1$ homogeneous stagnation solution will evolve. From Eq. (46), we determine the effective confinement time $t_0 \sim 0.236$ ns, and, from Eq. (47), we determine the stagnation time $t_i \sim 0.86$ ns. We now consider the time evolution of the on-axis density. From Eqs. (30) and (36), $\rho(r=0,t) = \rho_f/h(t)^2$, where the peak density ρ_f is determined by Eq. (44): $\rho_f = \rho_i e^{1/\epsilon_i} = (84.2\,\mathrm{kg/m^3})(28) \sim 2360\,\mathrm{kg/m^3}$. The time law $h(t)$ is determined by $t(h)$ in Eq. (38). Rather than attempting to invert this relation to obtain $h(t)$, we determine $\rho(t)$ parametrically by plotting the pair $(t(h), \rho(h) = \rho_f/h^2)$, where $t(h) = -t_0\sqrt{\frac{\pi}{2}}\mathrm{erfi}(\sqrt{\ln h})$.

However, to compare to the 3D simulation, we must add a time offset to $t(h)$. Recall that in the stagnation solution, the peak compression is assumed to occur at $t=0$, a time interval t_i after the initial time. We chose t = −1 ns in the 3D simulation as the initial time, and determined $t_i \sim 0.86$ ns. Hence, the stagnation solution predicts peak compression will occur at $-1+0.86=-0.14$ ns (in the time scale used in the 3D simulation), and we must add this time offset to $t(h)$:

$$t(h) = -1.4\times 10^{-10} - (2.36\times 10^{-10})\sqrt{\frac{\pi}{2}}\mathrm{erfi}\left(\sqrt{\ln h}\right). \quad (50)$$

The determination of $p(t)$ follows similarly. From Eqs. (31) and (36), for a $\gamma_{eff}\sim 1$ plasma, the on-axis pressure follows $p(t)=p_f/h(t)^2$, where peak pressure p_f is determined by $p_f = p_i h_i^2 = p_i e^{1/\epsilon_i} \sim 1.09e14$ J/m^3. Hence, $p(t)$ is determined by $(t(h), p(h)=1.09e14/h^2)$, where $t(h)$ is given by Eq. (50). Finally, to determine the slope of the velocity $m(t)$, we use Eq. (39) to obtain $m(h)=4.24e9\sqrt{2\ln h}/h$.

These theoretical predictions $\rho(t), p(t), m(t)$ are compared with their 3D counterparts in Fig. 11. The duration of the compression phase t_i is similar in the 3D simulation and isothermal stagnation solution. However, the latter compresses much more deeply than in 3D, achieving higher density and pressure.

B. $\gamma_{eff}\sim 1$, isothermal homogeneous stagnation with enhanced ϵ_i

As seen in Sec. II E, during compression, the core plasma exhibits significant centrifugal force, which aids the thermal pressure in resisting compression. Hence, it is reasonable that the 1D isothermal stagnation solution, which only accounts for the thermal pressure, exhibits higher compression than the 3D simulation. In the stagnation solution, the role of thermal pressure is captured by the parameter $\epsilon_i = \int p dV / \int \frac{1}{2}\rho v^2 dV$. As the initial pressure p increases, ϵ_i increases, and the compression decreases (see Eq. (44)). We surmise that the "hydrodynamic pressure" due to non-radial velocity terms, as discussed in Sec. II E, leads to an effectively higher ϵ_i, thus decreasing peak compression.

Let us consider an enhanced value of $\epsilon_i = 0.55$ while keeping $R_i = 0.267$ mm and $U_i = -3.9e5$ m/s, the same as in Sec. VI A. The enhanced ϵ_i results in lower peak density $\rho_f = \rho_i e^{1/\epsilon_i} = (84.2\,\mathrm{kg/m^3})(6.16) = 518.7\,\mathrm{kg/m^3}$ and pressure $p_f = p_i e^{1/\epsilon_i} = 2.4e13\,\mathrm{J/m^3}$. Also, the effective confinement time $t_0 = 0.37$ ns is enhanced, and the stagnation time $t_i = 0.7$ ns is slightly reduced. Consequently, the time offset discussed in Sec. VI A is modified to $-1+0.7=-0.3$ ns, resulting in

$$t(h) = -3\times 10^{-10} - (3.7\times 10^{-10})\sqrt{\frac{\pi}{2}}\mathrm{erfi}\left(\sqrt{\ln h}\right). \quad (51)$$

In exactly the same way as before, we determine $\rho(t)$, $p(t)$, $m(t)$, which are illustrated in Fig. 18. The enhanced pressure associated with $\epsilon_i = 0.55$ results in much better agreement with the 3D simulation.

Although the stagnation solution with enhanced ϵ_i is able to describe the compression of on-axis plasma, it cannot completely describe the dynamics of the stagnating core. In particular, the homogeneous stagnation assumes a hydrodynamically "isolated" plasma, with a fixed amount of internal and kinetic energy. In contrast, in 3D simulation, the stagnating core is constantly bombarded by imploding plasma, which adds internal and kinetic energy into the core as it accretes on the boundary, just as in the shock solution. Consequently, while the homogeneous stagnation describes the compression on axis for $t \le -0.3$ ns, during this same time interval, the shock solution better describes the growth of the core boundary, as seen in Fig. 17(b) and discussed in Sec. V B. Hence, comparison of 1D theory to 3D simulation can be tricky: different theories may simultaneously describe different aspects of the plasma.

VII. ROLE OF MAGNETIC FIELD AT STAGNATION

In Ref. 40, the authors argue from experimental considerations that the magnetic pressure p_B is not important in the overall pressure balance at stagnation, which is dominated by p and p_{ram}. Figures 3 and 4 support this claim, with $\beta = p_0/p_{B,0} \sim 5$, where p_0 and $p_{B,0}$ are the peak plasma pressure and magnetic pressure, respectively, at a given time. The core only carries a fraction of the full current, with the remainder flowing in the imploding plasma. For instance, at t = 0.4 ns, the core (defined by $R_{p=1e12}$) only carries 6 MA of the full 11 MA. We emphasize that $\beta \gg 1$ probably does not hold in strongly radiating systems, which cannot sustain high core pressures. Furthermore, lower pressure results in higher compression and higher $p_B \propto 1/r^2$.

Returning to the radiation-free case, we now consider how B affects the two solutions used to interpret the 3D simulations. First, the homogeneous, isothermal stagnation considered in Sec. IV B can be generalized to the ideal MHD equivalent by adding an azimuthal magnetic field B_θ.[15–17] This field further compresses the plasma relative to the $B_\theta = 0$ case, by an amount determined by β. For $\beta \sim 5$, the additional compression is very small relative to the $B_\theta = 0$ case, so we do not introduce significant error by ignoring B_θ.

Regarding the shock solution, we may also generalize to the ideal MHD case, as done by Velikovich *et al.*[71] Whereas in the $B_\theta = 0$ case, an unshocked fluid element travels towards axis with a constant velocity, in the $B_\theta \neq 0$ case, the fluid element accelerates inwards. However, looking at Fig. 3(c), the flat portion of the velocity profile rises very little with time, so the acceleration is not significant over the relatively short stagnation time.

Finite B_θ will also modify the shock solution by reducing the shock compression, as is well known (cf. Ref. 74). To estimate the reduction, we require the plasma beta in the unshocked plasma $\beta_1 = \frac{p_1}{B_{\theta 1}^2/2\mu_0}$ and Mach number $M = u_1/c_{s1}$. Here, u_1 is the velocity of the imploding plasma in the frame of the expanding shock, and c_{s1} is the sound speed in the imploding plasma. In the phase 2 imploding plasma, which is when the 3D simulation exhibits the shock solution, $M \sim 11$, $\beta_1 \sim 0.3, \gamma \sim 1.3$ are typical values. For these values, the shock jump $\rho_2/\rho_1 \sim 4.5$, while in the equivalent $B_\theta = 0$ case, $\rho_2/\rho_1 \sim 7.3$. Hence, finite B_θ can definitely reduce the shock compression. However, we do not expect this to significantly alter our conclusions.

Finally, during the short (<3 ns) time interval during which plasma stagnates on axis, we do not see the gross development of MHD instabilities in the core. This observation is consistent with an estimate of the MHD instability time $R/v_A \sim 1.3$ ns, where R is the core radius and v_A is the Alfven velocity at $r = R$.

VIII. CONCLUSION AND DISCUSSION

In this work, we investigated the connection between 3D MHD simulation, which may realistically model the plasma but can be difficult to physically interpret, and 1D theory. In particular, we focused on two 1D stagnation solutions: a strong shock scenario based off the Noh solution (Sec. IV A) and a homogeneous (i.e. shockless) stagnation (Sec. IV B). Comparison between 1D theory and 3D simulation is nontrivial due to 3D spatial non-uniformity. For instance, we cannot observe a clear shock boundary in the axially and azimuthally averaged 3D profiles, due to the shock occurring at different locations at a given time. Nonetheless, the time evolution of axially averaged, on-axis density ρ and pressure p, as well as the slope of the radial velocity profile, m, are useful for comparison to theory. Furthermore, the axially and azimuthally averaged pressure profile provides a reasonable estimate of the shock radius $R_p(t)$ (Sec. V B).

These metrics suggest that in 3D stagnation, the initial accumulation of material near axis does not possess sufficient azimuthal symmetry for the 1D shock solution to be realized in a global sense. Relative to the "equivalent" 1D simulation in Sec. III (which *does* exhibit a well-defined shock), the off-axis, oblique collisions in 3D result in a larger, lower density core with significant residual kinetic energy. The agreement of on-axis $\rho(t)$, $p(t)$, $m(t)$ with the homogeneous stagnation solution through the compression phase ($t \leq 0$ ns) suggest the residual radial kinetic energy near axis is transformed to internal energy in a nearly shockless fashion. However, this solution must be modified to account for the additional effective pressure (i.e., centrifugal force) and enhanced thermal transport driven by vortical flow in the core.

Once the on-axis density reaches its maximum at $t = 0$ ns, the stagnated plasma expands outward into the imploding plasma. The resulting decrease in on-axis ρ,p,m, as well as the growth in core boundary $R_p(t)$, qualitatively agree with both the analytic shock solution and the equivalent 1D simulation. Recall that during the initial phase of stagnation, imploding plasma jets collide obliquely, resulting in complicated flows that are difficult to describe in 1D. However, later in time ($t > 0$ ns), a high-pressure core has formed on axis, and the imploding jets collide with the core rather than each other. Such a core-jet interaction is better suited to 1D shock analysis. This behavior, combined with decaying vortical motion in the core, leads to improved agreement between 3D simulation, 1D simulation, and shock theory. However, during this time, we still cannot ignore the 3D nature of the flow: unlike the equivalent 1D simulation, in 3D, the core does not cool during expansion, which we postulate is due to "channels" of plasma that carry heat and kinetic energy to the core center (Sec. II D).

In conclusion, 1D stagnation solutions are useful in interpreting and understanding 3D simulation, despite the highly inhomogeneous flows observed there. In turn, 3D simulation enlightens our usage of 1D theory: the 3D flows suggest enhanced thermal transport as well as effectively enhanced pressure, due to centrifugal forces.

Even within the confines of this restricted study (i.e. no radiation loss), many possibilities exist for future study, including the role of axial flow (essentially ignored here), as well as the mechanism by which the vortices dissipate. Furthermore, the shear flows observed in Figs. 5 and 8, combined with large Reynolds number ($Re = ul/\nu_i \sim$ (2e5 m/s)(4e-4 m)/(1e-6 m^2/s) $\sim$8e7) suggest the core is fertile ground for turbulence, which will affect pressure balance through the Reynolds stress tensor (see Refs. 75 and 76, and references therein). However, the resulting small length scales (e.g., Taylor microscale $\sim l/\sqrt{Re} \sim$ 5e–8m) are beyond the scope of these simulations, which use 20 μm zoning to remain tractable.

In this work, we focused on a specific wire-array configuration of fixed radius (1 cm), mass (1.15 mg), and material (tungsten). It remains for future work to generalize to different array configurations, as well as see how our conclusions change when we allow radiation loss. Nonetheless, we have achieved a deeper understanding of large-scale flow at stagnation that will be helpful in understanding 3D stagnation in wire arrays, and possibly other high-energy-density systems. Furthermore, we hope that the metrics developed here for comparison between 3D simulation and theory may be extended to experiments in which the radiative losses are low. For instance, measurement of the pre-stagnation density and velocity profiles determine the unknowns χ and λ required by the shock theory. We could then compare the evolution of on-axis density during stagnation with shock theory $(\rho(t) \propto t^{\frac{2\chi}{1+\lambda}})$, as well as the shock radius growth $(R_p(t) \propto t^{\frac{1}{1+\lambda}})$.

ACKNOWLEDGMENTS

E.P.Y. thanks C. Nakhleh, D. Flicker, M. Herrmann, and K. Peterson for programmatic support; T. Haill for ALEGRA guidance; and T. Awe for help with the figures. We are indebted to D. Sinars, K. Peterson, and M. Cuneo for reviewing the paper and providing very helpful suggestions. We thank D. Ampleford, D. Bliss, A. Chuvatin, S. Hansen, C. Jennings, B. Jones, R. Lemke, T. Mehlhorn, L. Rudakov, R. Vesey, and E. Waisman for stimulating discussion. Finally, we are grateful to ALEGRA Code Development Team (in particular, W. Rider, A. Robinson, C. Siefert, and C. Ober) for making these simulations possible. Sandia is a multiprogram laboratory operated by Sandia Corporation, a Lockhead Martin Company, for the National Nuclear Security Administration under DE-AC04-94AL85000.

APPENDIX: ENERGY FLOW IN THE Z PINCH

Energy flow in a Z pinch can be visualized in cartoon-fashion as water flowing through a series of buckets and pipes, as illustrated in Fig. 21. The spigot at the top represents the generator, and the water level in each bucket

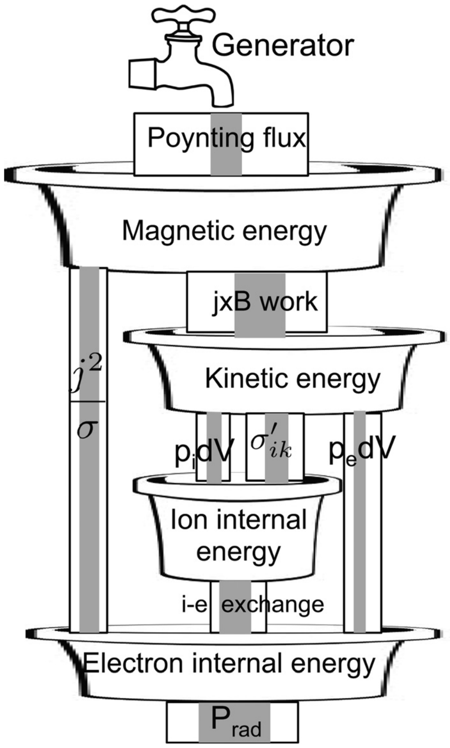

FIG. 21. Visualization of energy flow in a Z pinch.

represents the amount of magnetic, kinetic, or internal energy in the system at a given time. The rate at which the water level in a given bucket varies is determined by the flow of water into and out of the bucket through the connecting pipes, which represent energy conversion mechanisms. In this way, we can visualize the flow of water from the spigot to the magnetic energy bucket, which then flows into the kinetic energy bucket during the implosion phase. At stagnation, the kinetic energy converts into ion and electron internal energy, which is then radiated away. We now examine each phase of the above process in more detail.

The spigot (i.e., generator) supplies Poynting flux to the system. The Poynting theorem, combined with the MHD Ohm's law $\mathbf{E}+\mathbf{v}\times\mathbf{B}=\eta\,\mathbf{j}$ yields

$$\frac{\partial}{\partial t}\int\frac{B^2}{2\mu_0}dV=-\int(\mathbf{E}\times\mathbf{H})\cdot d\mathbf{S}-\int\mathbf{v}\cdot(\mathbf{j}\times\mathbf{B})dV-\int\frac{j^2}{\sigma}dV,$$

in which we have integrated over a fixed volume enclosing the plasma. Physically, we can interpret this equation as follows: Poynting flux through the surface of the volume (2nd term) increases the magnetic energy (1st term), which itself is reduced by performing work on accelerating the plasma (3rd term) as well as through Ohmic dissipation (4th term). In terms of Fig. 21, the rate at which energy builds up in the magnetic energy equals the rate at which energy flows from the generator (via Poynting flux) minus the rate at which magnetic energy is lost through the two pipes exiting the bucket, corresponding to Ohmic dissipation and $\mathbf{j}\times\mathbf{B}$ work done on the plasma.

This $\mathbf{j}\times\mathbf{B}$ work increases the kinetic energy of the plasma, the rate of increase of which is described by the kinetic energy equation, integrated over the plasma volume:

$$\frac{\partial}{\partial t}\int\frac{1}{2}\rho v^2dV=\int\mathbf{v}\cdot(\mathbf{j}\times\mathbf{B})dV-\int\sigma'_{ik}\frac{\partial v_i}{\partial x_k}dV+\int(p_i+p_e)(\nabla\cdot\mathbf{v})dV,$$

where p_i and p_e are the ion and electron pressures, respectively, and $\sigma_{ik}{}'$ is the viscosity tensor. In words, the rate at which plasma kinetic energy increases (1st term) is determined by the rate at which $\mathbf{j}\times\mathbf{B}$ work is done on the plasma (2nd term) minus the rate at which kinetic energy is dissipated through viscosity (3rd term) and converted to plasma internal energy through pdV work (4th term). Of course, the last term can also increase the kinetic energy if the plasma is expanding. Referring back to Fig. 21, the rate at which energy builds up in the kinetic energy bucket equals the rate at which magnetic energy is converted through the $\mathbf{j}\times\mathbf{B}$ "pipe" minus the rate at which kinetic energy converts to internal energy through the pdV and viscous dissipation pipes.

The ion energy equation can be written as

$$\frac{\partial}{\partial t}\int\rho e_idV=-\int p_i\nabla\cdot\mathbf{v}dV+\int\sigma'_{ik}\frac{\partial v_i}{\partial x_k}dV+\int\frac{3}{2}n_ek_b\frac{T_e-T_i}{\tau_{eq}}dV,$$

where the first term represents the rate of change of ion internal energy. The second term describes how the ion internal energy increases as the plasma compresses on axis, due to p_idV work. The third term accounts for the increase in internal energy as the kinetic energy is dissipated by viscosity during collisions. The final term is the ion-electron energy exchange term.

Last, the electron energy equation yields

$$\frac{\partial}{\partial t}\int\rho e_edV=-\int p_e\nabla\cdot\mathbf{v}dV-\int\frac{3}{2}n_ek_b\frac{T_e-T_i}{\tau_{eq}}dV+\int\frac{j^2}{\sigma}dV-P_{rad},$$

where the first two terms are the electron analog to the first two terms in the ion energy equation. The fourth and fifth terms represent Joule heating and radiation loss, respectively.

[1]K. G. Whitney, J. W. Thornhill, J. P. Apruzese, J. Davis, C. Deeney, and C. A. Coverdale, Phys. Plasmas **11**, 3700 (2004).

[2]V. L. Kantsyrev, L. I. Rudakov, A. S. Safronova, D. A. Fedin, V. V. Ivanov, A. L. Velikovich, A. A. Esaulov, A. S. Chuvatin, K. Williamson, N. D. Ouart, V. Nalajala, G. Osborne, I. Shrestha, M. F. Yilmaz, S. Pokala, P. J. Laca, and T. E. Cowan, IEEE Trans. Plasma Sci. **34**, 2295 (2006).

[3]M. G. Haines, P. D. LePell, C. A. Coverdale, B. Jones, C. Deeney, and J. P. Apruzese, Phys. Rev. Lett. **96**, 075003 (2006).

[4]L. I. Rudakov, A. L. Velikovich, J. Davis, J. W. Thornhill, J. L. Giuliani, Jr., and C. Deeney, Phys. Rev. Lett. **84**, 3326 (2000).

[5]A. L. Velikovich, J. Davis, J. W. Thornhill, J. L. Giuliani, Jr., L. I. Rudakov, and C. Deeney, Phys. Plasmas **7**, 3265 (2000).

[6]D. L. Peterson, R. L. Bowers, K. D. McLenithan, C. Deeney, G. A. Chandler, R. B. Spielman, M. K. Matzen, and N. F. Roderick, Phys. Plasmas **5**, 3302 (1998).

[7]J. P. Chittenden, S. V. Lebedev, C. A. Jennings, S. N. Bland, and A. Ciardi, Plasma Phys. Controlled Fusion **46**, B457 (2004).
[8]C. A. Jennings, M. E. Cuneo, E. M. Waisman, D. B. Sinars, D. J. Ampleford, G. R. Bennett, W. A. Stygar, and J. P. Chittenden, Phys. Plasmas **17**, 092703 (2010).
[9]E. Kroupp, D. Osin, A. Starobinets, V. Fisher, B. Bernshtam, Y. Maron, I. Uschmann, E. Förster, A. Fisher, and C. Deeney, Phys. Rev. Lett. **98**, 115001 (2007).
[10]D. B. Sinars, R. W. Lemke, M. E. Cuneo, S. V. Lebedev, E. M. Waisman, W. A. Stygar, B. Jones, M. C. Jones, E. P. Yu, J. L. Porter, and D. F. Wenger, Phys. Rev. Lett. **100**, 145002 (2008).
[11]V. V. Ivanov, V. I. Sotnikov, J. M. Kindel, P. Hakel, R. C. Mancini, A. L. Astanovitskiy, A. Haboub, S. D. Altemara, A. P. Shevelko, E. D. Kazakov, and P. V. Sasorov, Phys. Rev. E. **79**, 056404 (2009).
[12]J. E. Allen, Proc. Phys. Soc., London, Sect. B **70**, 24 (1957).
[13]D. Potter, Nucl. Fusion **18**, 813 (1978).
[14]T. Miyamoto, Nucl. Fusion **24**, 337 (1984).
[15]A. G. Kulikovskii, Dokl. Akad. Nauk SSSR **114**, 984 (1957) [In Russian].
[16]F. S. Felber, Phys. Fluids **25**, 643 (1982).
[17]L. S. Solov'ev, Sov. J. Plasma Phys. **10**, 602 (1984).
[18]B. E. Meierovich, Sov. J. Plasma Phys. **11**, 831 (1985).
[19]M. A. Liberman and A. L. Velikovich, Nucl. Fusion **26**, 709 (1986).
[20]M. Tendler, Phys. Fluids **31**, 3449 (1988).
[21]M. M. Basko, P. V. Sasorov, M. Murakami, V. G. Novikov, and A. S. Grushin, Plasma Phys. Controlled Fusion **54**, 055003 (2012).
[22]S. V. Lebedev, D. J. Ampleford, S. N. Bland, S. C. Bott, J. P. Chittenden, J. Goyer, C. Jennings, M. G. Haines, G. N. Hall, D. A. Hammer, J. B. A. Palmer, S. A. Pikuz, T. A. Shelkovenko, and T. Christoudias, Plasma Phys. Controlled Fusion **47**, A91 (2005).
[23]M. E. Cuneo, E. M. Waisman, S. V. Lebedev, J. P. Chittenden, W. A. Stygar, G. A. Chandler, R. A. Vesey, E. P. Yu, T. J. Nash, D. E. Bliss, G. S. Sarkisov, T. C. Wagoner, G. R. Bennett, D. B. Sinars, J. L. Porter, W. W. Simpson, L. E. Ruggles, D. F. Wenger, C. J. Garasi, B. V. Oliver, R. A. Aragon, W. E. Fowler, M. C. Hettrick, G. C. Idzorek, D. Johnson, K. Keller, S. E. Lazier, J. S. McGurn, T. A. Mehlhorn, T. Moore, D. S. Nielsen, J. Pyle, S. Speas, K. W. Struve, and J. A. Torres *et al.*, Phys. Rev. E **71**, 046406 (2005).
[24]M. E. Cuneo, D. B. Sinars, E. M. Waisman, D. E. Bliss, W. A. Stygar, R. A. Vesey, R. W. Lemke, I. C. Smith, P. K. Rambo, J. L. Porter, G. A. Chandler, T. J. Nash, M. G. Mazarakis, R. G. Adams, E. P. Yu, K. W. Struve, T. A. Mehlhorn, S. V. Lebedev, J. P. Chittenden, and C. A. Jennings, Phys. Plasmas **13**, 056318 (2006).
[25]D. B. Sinars, M. E. Cuneo, B. M. Jones, C. A. Coverdale, T. J. Nash, M. G. Mazarakis, J. L. Porter, C. Deeney, D. F. Wenger, R. G. Adams, E. P. Yu, D. E. Bliss, and G. S. Sarkisov, Phys. Plasmas **12**, 056303 (2005).
[26]V. V. Aleksandrov, E. V. Grabovskii, G. G. Zukakishvili, M. V. Zurin, N. N. Komarov, I. V. Krasovsky, K. N. Mitrofanov, S. L. Nedoseev, G. M. Oleinik, I. Yu. Porofeev, A. A. Samokhin, P. V. Sasorov, V. P. Smirnov, M. V. Fedulov, I. N. Frolov, and A. A. Chernov, J. Exp. Theor. Phys. **97**, 745 (2003).
[27]M. G. Haines, Plasma Phys. Control. Fusion **53**, 093001 (2011).
[28]E. Kroupp, D. Osin, A. Starobinets, V. Fisher, V. Bernshtam, L. Weingarten, Y. Maron, I. Uschmann, E. Förster, A. Fisher, M. E. Cuneo, C. Deeney, and J. L. Giuliani, Phys. Rev. Lett. **107**, 105001 (2011).
[29]K. G. Whitney, J. W. Thornhill, J. P. Apruzese, and J. Davis, J. Appl. Phys. **67**, 1725 (1990).
[30]J. W. Thornhill, K. G. Whitney, and J. Davis, J. Quant. Spectrosc. Radiat. Transf. **44**, 251 (1990).
[31]J. W. Thornhill, K. G. Whitney, C. Deeney, and P. D. Lepell, Phys. Plasmas **1**, 321 (1994).
[32]K. G. Whitney, J. W. Thornhill, J. L. Giuliani, Jr., J. Davis, L. A. Miles, E. E. Nolting, V. L. Kenyon, W. A. Speicer, J. A. Draper, C. R. Parsons, P. Dang, R. B. Spielman, T. J. Nash, J. S. McGurn, L. E. Ruggles, C. Deeney, R. R. Prasad, and L. Warren, Phys. Rev. E **50**, 2166 (1994).
[33]B. Jones, C. Deeney, C. A. Coverdale, P. D. Lepell, J. L. McKenney, J. P. Apruzese, J. W. Thornhill, K. G. Whitney, R. W. Clark, A. L. Velikovich, J. Davis, Y. Maron, V. Kantsyrev, A. Safronova, and V. I. Oreshkin, J. Quant. Spectrosc. Radiat. Transf. **99**, 341 (2006).
[34]V. I. Oreshkin, AIP Conf. Proc. **409**, 215 (1997); "Radiative MHD modeling of implosions of plasma liners," preprint no. 4, High Current Electronics Institute, Tomsk, Russia, 1994 in Russian; V. I. Oreshkin, Russ. Phys. J **38**, 1203 (1995).
[35]A. S. Chuvatin, L. I. Rudakov, A. L. Velikovich, J. Davis, and V. I. Oreshkin, IEEE Trans. Plasma Sci. **33**, 739 (2005).
[36]B. Jones, C. A. Jennings, D. C. Lamppa, S. B. Hansen, A. J. Harvey-Thompson, D. J. Ampleford, M. E. Cuneo, T. Strizic, D. Johnson, M. C. Jones, N. W. Moore, T. M. Flanagan, J. L. McKenney, E. M. Waisman, C. A. Coverdale, M. Krishnan, P. L. Coleman, K. W. Elliot, R. E. Madden, J. Thompson, A. Bixler, J. W. Thornhill, J. L. Giuliani, Y. K. Chong, A. L. Velikovich, A. Dasgupta, and J. P. Apruzese, IEEE Trans. Plasma Sci. **42**, 1145 (2014).
[37]A. L. Velikovich, R. W. Clark, J. Davis, Y. K. Chong, C. Deeney, C. A. Coverdale, C. L. Ruiz, G. W. Cooper, A. J. Nelson, J. Franklin, and L. I. Rudakov, Phys. Plasmas **14**, 022701 (2007).
[38]C. A. Coverdale, C. Deeney, A. L. Velikovich, R. W. Clark, Y. K. Chong, J. Davis, J. Chittenden, C. L. Ruiz, G. W. Cooper, A. J. Nelson, J. Franklin, P. D. LePell, J. P. Apruzese, J. Levine, J. Banister, and N. Qi, Phys. Plasmas **14**, 022706 (2007).
[39]C. A. Coverdale, C. Deeney, A. L. Velikovich, J. Davis, R. W. Clark, Y. K. Chong, J. Chittenden, S. Chantrenne, C. L. Ruiz, G. W. Cooper, A. J. Nelson, J. Franklin, P. D. LePell, J. P. Apruzese, J. Levine, and J. Banister, Phys. Plasmas **14**, 056309 (2007).
[40]Y. Maron, A. Starobinets, V. I. Fisher, E. Kroupp, D. Osin, A. Fisher, C. Deeney, C. A. Coverdale, P. D. Lepell, E. P. Yu, C. Jennings, M. E. Cuneo, M. C. Herrmann, J. L. Porter, T. A. Mehlhorn, and J. P. Apruzese, Phys. Rev. Lett. **111**, 035001 (2013).
[41]J. P. Apruzese, J. L. Giuliani, J. W. Thornhill, C. A. Coverdale, B. Jones, and D. J. Ampleford, Phys. Plasmas **20**, 022707 (2013).
[42]R. Betti, R. Nora, A. Christopherson, and P. Radha, presentation at the Cryo Workshop, Laboratory for Laser Engineering, University of Rochester, April 29–30, (unpublished).
[43]A. Yu. Labetsky, R. B. Baksht, V. I. Oreshkin, A. G. Rousskikh, and A. V. Shishlov, IEEE Trans. Plasma Sci. **30**, 524 (2002).
[44]S. A. Chaikovsky, A. Yu. Labetsky, V. I. Oreshkin, A. V. Shishlov, R. B. Baksht, A. V. Fedunin, and A. G. Rousskikh, Laser Part. Beams **21**, 255 (2003).
[45]A. V. Shishlov, R. B. Baksht, S. A. Chaikovsky, A. V. Fedunin, F. I. Fursov, V. A. Kokshenev, N. E. Kurmaev, A. Yu. Labetsky, V. I. Oreshkin, N. A. Ratakhin, A. G. Rousskikh, and S. V. Shlykhtun, Laser Phys. **16**, 183 (2006).
[46]H. Sze, J. Banister, B. H. Failor, J. S. Levine, N. Qi, A. L. Velikovich, J. Davis, D. Lojewski, and P. Sincerny, Phys. Rev. Lett. **95**, 105001 (2005).
[47]J. S. Levine, J. Banister, B. H. Failor, N. Qi, H. Sze, A. L. Velikovich, R. J. Commisso, J. Davis, and D. Lojewski, Phys. Plasmas **13**, 082702 (2006).
[48]H. Sze, J. S. Levine, J. Banister, B. H. Failor, N. Qi, P. Steen, A. L. Velikovich, J. Davis, and A. Wilson, Phys. Plasmas **14**, 056307 (2007).
[49]D. Osin, E. Kroupp, A. Starobinets, G. Rosenzweig, D. Alumot, Y. Maron, A. Fisher, E. Yu, J. L. Giuliani, and C. Deeney, IEEE Trans. Plasma Sci. **39**, 2392 (2011).
[50]R. D. McBride, M. R. Martin, R. W. Lemke, J. B. Greenly, C. A. Jennings, D. C. Rovang, D. B. Sinars, M. E. Cuneo, M. C. Herrmann, S. A. Slutz, C. W. Nakhleh, D. D. Ryutov, J. P. Davis, D. G. Flicker, B. E. Blue, K. Tomlinson, D. Schroen, R. M. Stamm, G. E. Smith, J. K. Moore, T. J. Rogers, G. K. Robertson, R. J. Kamm, I. C. Smith, M. Savage, W. A. Stygar, G. A. Rochau, M. Jones, M. R. Lopez, J. L. Porter, and M. K. Matzen, Phys. Plasmas **20**, 056309 (2013).
[51]T. J. Awe, R. D. McBride, C. A. Jennings, D. C. Lamppa, M. R. Martin, D. C. Rovang, S. A. Slutz, M. E. Cuneo, A. C. Owen, D. B. Sinars, K. Tomlinson, M. R. Gomez, S. B. Hansen, M. C. Herrmann, J. L. McKenney, C. Nakhleh, G. K. Robertson, G. A. Rochau, M. E. Savage, D. G. Schroen, and W. A. Stygar, Phys. Rev. Lett. **111**, 235005 (2013).
[52]V. A. Thomas and R. J. Kares, Phys. Rev. Lett. **109**, 075004 (2012).
[53]See Supplementary material at http://dx.doi.org/10.1063/1.4891844 for the derivations and formulas not included in the main text.
[54]W. F. Noh, J. Comput. Phys. **72**, 78 (1987).
[55]A. C. Robinson and C. J. Garasi, Comput. Phys. Commun. **164**, 408 (2004).
[56]M. P. Desjarlais, J. D. Kress, and L. A. Collins, Phys. Rev. E **66**, 025401(R) (2002).
[57]E. P. Yu, B. V. Oliver, P. V. Sasorov, D. B. Sinars, T. A. Mehlhorn, M. E. Cuneo, M. G. Haines, and S. V. Lebedev, Phys. Plasmas **14**, 022705 (2007).
[58]E. P. Yu, M. E. Cuneo, M. P. Desjarlais, R. W. Lemke, D. B. Sinars, T. A. Haill, E. M. Waisman, G. R. Bennett, C. A. Jennings, T. A. Mehlhorn, T. A. Brunner, H. L. Hanshaw, J. L. Porter, W. A. Stygar, and L. I. Rudakov, Phys. Plasmas **15**, 056301 (2008).
[59]R. W. Lemke, D. B. Sinars, E. M. Waisman, M. E. Cuneo, E. P. Yu, T. A. Haill, H. L. Hanshaw, T. A. Brunner, C. A. Jennings, W. A. Stygar, M. P. Desjarlais, T. A. Mehlhorn, and J. L. Porter, Phys. Rev. Lett. **102**, 025005 (2009).

[60]S. N. Bland, S. V. Lebedev, J. P. Chittenden, G. N. Hall, F. Suzuki-Vidal, D. J. Ampleford, S. C. Bott, J. B. A. Palmer, S. A. Pikuz, and A. Shelkovenko, Phys. Plasmas **14**, 056315 (2007).
[61]D. D. Ryutov, M. S. Derzon, and M. K. Matzen, Rev. Mod. Phys. **72**, 167 (2000).
[62]K. Hiemenz, Dinglers Polytech. J. **326**, 311 (1911).
[63]E. R. Priest, *Solar Magnetohydrodynamics* (Reidel, Dordrecht, 1982), p. 85.
[64]Ya. B. Zel'dovich and Yu. P. Raizer, *Physics of Shock Waves and High-Temperature Hydrodynamic Phenomena* (Dover, New York, 2002).
[65]R. P. Drake, *High-Energy-Density Physics* (Springer, Berlin Heidelberg New York, 2006).
[66]S. Atzeni and J. Meyer-ter-Vehn, *The Physics of Inertial Fusion* (Clarendon, Oxford, 2004).
[67]G. Barenblatt, *Similarity, Self-Similarity, and Intermediate Asymptotics* (Consultants Bureau, New York, 1979).
[68]L. I. Sedov, *Similarity and Dimensional Methods in Mechanics* (Pergamon, New York, 1960).
[69]G. Guderley, Luftfahrtforschung **19**, 301 (1942).
[70]K. P. Stanyukovich, *Unsteady Motion of Continuous Media* (Academic Press, New York, 1960).
[71]A. L. Velikovich, J. L. Giuliani, S. T. Zalesak, J. W. Thornhill, and T. A. Gardiner, Phys. Plasmas **19**, 012707 (2012).
[72]R. Lazarus, SIAM J. Numer. Anal. **18**, 316 (1981); Errata, *ibid.* **19**, 1090 (1982).
[73]A. L. Velikovich and J. Davis, Phys. Plasmas **2**, 4513 (1995).
[74]T. J. M. Boyd and J. J. Sanderson, *The Physics of Plasmas* (Cambridge University Press, Cambridge, 2003).
[75]G. Hazak, A. L. Velikovich, J. H. Gardner, and J. P. Dahlburg, Phys. Plasmas **5**, 4357 (1998).
[76]A. L. Velikovich, C. Huete, and J. G. Wouchuk, Phys. Rev. E **85**, 016301 (2012).